Journal of Environmental Chemical Engineering 13 (2025) 116811

Contents lists available at ScienceDirect

Journal of Environmental Chemical Engineering

journal homepage: www.elsevier.com/locate/jece

Integrating pyro- and biohydrometallurgy in a green closed-loop lithium-ion battery recycling approach

Lukas Wiszniewski [a,*], Lalropuia Lalropuia [b], Sabine Spiess [b], Peter Presoly [c], Klemens Kremser [d], Klaus Doschek-Held [a], Georg M. Guebitz [d], Zlatko Raonic [a]

[a] Montanuniversität Leoben, Chair of Thermal Processing Technology, Leoben, Austria
[b] K1-MET GmbH, Linz, Austria
[c] Montanuniversität Leoben, Chair of Ferrous Metallurgy, Leoben, Austria
[d] Department of Agrobiotechnology, IFA-Tulln, Institute of Environmental Biotechnology, BOKU University, Tulln an der Donau, Austria

ARTICLE INFO

Keywords:
Lithium-ion Batteries
Pyrometallurgy
Biohydrometallurgy
Recycling
Closed-loop

ABSTRACT

State-of-the-art stand-alone recycling routes for lithium-ion batteries (LIB), such as pyrometallurgy or hydrometallurgy, face significant challenges, including high energy consumption, loss of valuable elements like lithium (Li) and susceptibility to a waste stream with varying cathode chemistry. The present work investigates the comparison of recovery targets when processing synthesized black mass between a standalone biohydrometallurgical process and a combined method, including an upstream pyrometallurgical process. In this approach, black mass undergoes carbothermic reduction in the InduMelt reactor, in which volatile elements like Li are vaporized and extracted via the gas stream, producing a Li-free alloy. Thermodynamic equilibrium calculations using FactSage™ showed the possibility of partial oxidation when using the alloy in an open-loop approach. Within a closed-loop approach, the alloy was pulverized for downstream biohydrometallurgy. Bioleaching experiments using adapted enriched cultures with synthetic pre- and untreated NMC811 and LFP black mass were performed at pulp densities (w/v) of 1 % and 10 %. The highest leaching efficiency of up to 100 % for Nickel (Ni), Manganese (Mn), Cobalt (Co), and Aluminium (Al) was achieved in the 1 % pre-treated experiment. Increasing the pulp density to 10 % reduced the leaching efficiency of these metals to less than 25 % which could be attributed to factors such as the alkaline nature of the black mass, microbial inhibition and passivation due to precipitation. Pyrometallurgical pre-treatment improved metal leaching from NMC by up to 90 %, but had no impact on LFP. To close the materials loop, selective precipitation was applied.

1. Introduction

The demand for lithium-ion batteries (LIB) has seen an ever-growing rise, mainly caused by the desire for global electrification, touching diverse sectors, including the automotive industry and the broader transition towards sustainable energy solutions [1,2]. The rapid growth in the production and use of LIBs has consequently created a pressing need for efficient recycling methods to recover valuable metals such as lithium (Li), cobalt (Co), nickel (Ni), and other critical elements to avoid a resource dependency and mitigate environmental impacts. The European Union (EU) has recognized this urgency and has implemented stringent regulations to promote the recycling and recovery of these critical metals. The EU's Battery Directive mandates high collection and recycling rates for batteries with a special focus on LIBs, stipulating targets of 95 % for Ni, Co, and copper (Cu) and 80 % for Li until 2031 [3]. These regulations will drive innovation in recycling technologies, evaluating existing and emerging methods crucial for a sustainable battery life cycle. Demand forecasts, however, tend to be underestimated and are heavily adjusted upwards from time to time. While the anticipated global demand for LIBs was initially projected to be around 2.6 TWh in early 2020, a mere two years later, this forecast surged to 4.700 GWh by 2030 [1]. Furthermore, a fundamental transformation in the composition of cathode active materials (CAM) within LIBs has occurred, shifting from lithium-nickel-cobalt-aluminum-oxide (NCA) and low Ni- Nickel-Manganese-Cobalt-oxide (NMC) dominance to a market dominated by high Ni-NMC and lithium-iron-phosphate (LFP) chemistries (Fig. 1) [4]. This transformation is underpinned by the need for cost-effective stationary energy storage (represented by LFP cathode

* Correspondence to: Franz-Josef Straße 18, Leoben 8700, Austria.
E-mail address: lukas.wiszniewski@unileoben.ac.at (L. Wiszniewski).

https://doi.org/10.1016/j.jece.2025.116811
Received 16 October 2024; Received in revised form 24 April 2025; Accepted 25 April 2025
Available online 27 April 2025

chemistry) [5,6] and high-energy-density solutions for the mobility sector (represented by high Ni-NMC cathode materials) [7,8]. While the industry can readily adapt to these changing CAM requirements, this evolving landscape presents a significant challenge in efficiently and effectively managing these batteries' recycling [2].

The cathode is specially primed for recycling due to the high amount of scarce and strategically important elements like Li, Ni, Co, and Phosphorous (P) [10]. Current industrial recycling methods for LIBs primarily include pyrometallurgical and/or hydrometallurgical processes, each with distinct advantages and limitations [11,12]. Pyrometallurgical recycling is a well-established method that involves high-temperature processing to extract metals from LIBs. This method includes calcination, roasting, and smelting [13]. In calcination, LIB components are heated in an oxygen-deficient environment, leading to the decomposition of lithium-metal oxides and the release of volatile components [14]. Roasting, conducted in a low-oxygen atmosphere, facilitates gas-solid reactions that convert active cathode materials into simpler oxides [15,16]. The most critical stage, smelting, involves melting the materials at temperatures exceeding 1400 °C. This high-temperature treatment separates transition metals such as Ni, Co, Cu, Fe, and Mn from lighter elements typically found in the slag phase, such as aluminum (Al), calcium (Ca), and silicon (Si). This separation facilitates the formation of a metal-rich alloy and a mineral slag phase, where both can be efficiently processed in subsequent steps. While smelting is robust against impurities and can handle a waste stream of mixed battery chemistries, it is also energy-intensive and can generate toxic gases, necessitating extensive gas-cleaning systems. Moreover, Li often ends up in the slag, requiring additional steps for recovery, which are economically unfavorable in cases of low commodity prices for Li [13,17]. For example, Umicore's Battery Recycling Process in Belgium uses a sophisticated pyrometallurgical method to recover Co, Ni, and Cu, but additional hydrometallurgical steps are required to recover Li [18,19]. Additionally, to reuse the alloy for battery production within a closed-loop recycling approach, further downstream processes such as hydrometallurgy have to be deployed to achieve the desired product quality.

Hydrometallurgical processes involve aqueous chemistry to recover metals from LIBs [20]. These processes typically start with the pre-treatment of batteries, including discharging, dismantling, and crushing to liberate the active materials [21]. The resulting 'black mass', a mixture of the cathode – and anode active material (AAM) with several impurities, is subjected to leaching using organic or inorganic acids like oxalic acid ($C_2H_2O_4$) [22], sulfuric acid (H_2SO_4), hydrochloric acid (HCl), or nitric acid (HNO_3) [23,24]. Generally, hydrometallurgy is advantageous for its ability to recover Li efficiently and produce high-purity products either as metal hydroxides or as metal salts [25]. However, stringent safety measures are required to handle strong acids and oxidizers. Given the projected future waste streams, a highly fluctuating composition of materials can be expected where each additional element introduced into the recycling process increases hydrometallurgical methods' complexity and resource dependency. This variability complicates the extraction and purification processes, necessitating more advanced and resource-intensive techniques to recover valuable materials efficiently. As a result, managing these diverse waste streams becomes increasingly challenging, emphasizing the need for more adaptable and sustainable recycling solutions [26].

Biohydrometallurgical processes have gained increasing interest in recent years, with commercial applications already established for the biooxidation of refractory gold ores or concentrates, as well as bioleaching of low-grade sulphidic ores such as copper sulfides [27–29]. Bioleaching is a process by which metals from insoluble solids such as minerals and ores are solubilized using acidophilic bacteria or archaea, microorganisms thriving under acidic conditions. These microbes are mainly chemolithoautotrophs obtaining the energy required for growth via the oxidation of inorganic substances such as Fe^{2+}, H_2, reduced sulfur compounds, etc., and use CO_2 as their carbon source [30]. The primary role of these microorganisms in bioleaching is the production of ferric iron (Fe^{3+}) and H_2SO_4 through the oxidation of Fe^{2+} and reduced sulfur compounds, respectively, which then acts as an oxidant to solubilize metals into the leaching solution [31,32]. Recently, bioleaching has been broadened to other secondary sources such as electronic waste, spent LIBs, ashes, and slags from waste incineration, etc. [33–35]. Bioleaching processes, both electrochemically assisted and not, represent a promising, environmentally friendly alternative to conventional hydrometallurgical methods [36,37]. It operates at ambient temperatures and pressures, significantly reducing energy consumption and minimizing the production of hazardous byproducts [38]. However, these processes are slower than chemical leaching and require optimization of microbial cultures and conditions to achieve desirable metal recovery rates [39]. In addition, complex feedstock such as spent LIBs for bioleaching lead to complications such as high concentration of heavy metals, alkaline nature of the material, inhomogeneity of the material, etc., which may be toxic to the microorganisms and hinder the leachability of the metals.

Despite these advancements, there is growing interest in combining pyrometallurgical and downstream hydro- or biohydrometallurgical processes to leverage the strengths of both approaches. Generally, this paper investigates the comparative effectiveness and limitations of solely biohydrometallurgical processes versus a combined pyrometallurgical and biohydrometallurgical approach. For pyrometallurgical treatment of the black mass, the so-called InduRed reactor concept is used, enabling the evaporation of volatile elements via its favorable thermodynamic properties, leading to an almost Li- and P-free alloy. With the possibility of using renewable energies for the reduction

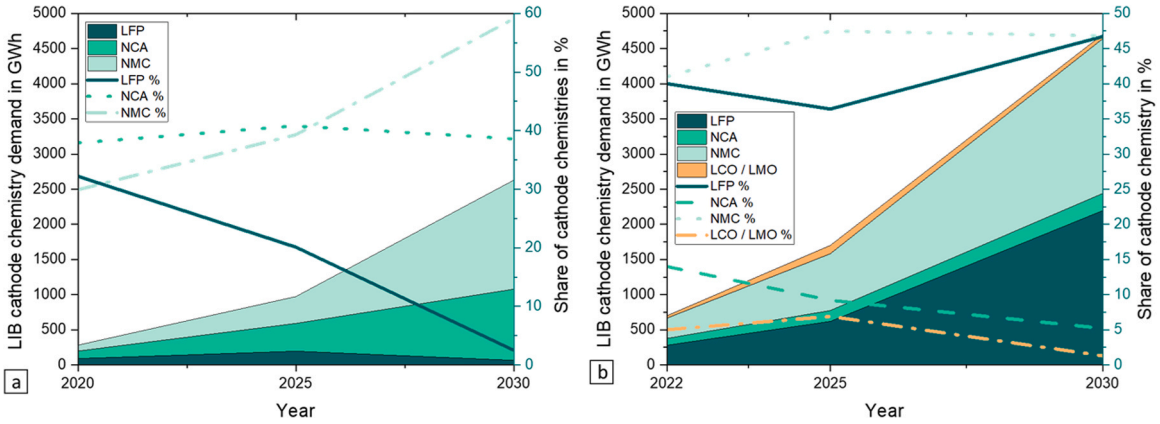

Fig. 1. LIB cathode chemistry demand forecast in GWh and respective shares of cathode chemistries; a.) forecast based on McKinsey numbers from 2020 and Xu et al. (2020) [8] b.) forecast based on McKinsey numbers from 2023 [6] and Pillot et al. (2023) [9] (Further details regarding the underlying data is given in Appendix A.).

processes of the oxidic input material, the environmental impact can be reduced drastically by decreasing the need for conventional energy sources and, therefore, limiting the amount of greenhouse gas emissions. Further treatment of the alloy using direct biohydrometallurgical leaching also benefits the ecological impact by supporting process simplicity and, therefore, energy and cost efficiency as well as speed and control since the process directly relies on the natural metabolic processes of the microorganisms. To close the loop of Li-ion battery recycling, purification and metal separation of the metal burden (bio) leachates are crucial. Currently, different technologies such as biosorption [40], electrowinning [41], bioelectrochemical metal recovery [42], solvent extraction [43], and selective precipitation [44] are being investigated. Regarding the latter, metals are precipitated by adding precipitation agents such as sodium hydroxide, lime, or sodium carbonate, raising the pH till the solubility limit is exceeded. Hydroxide precipitation is widely used in industry and is a relatively inexpensive, easy to implement method and was thus the method of choice in this work for purification [45].

This study seeks to comprehensively assess these novel and yet unexplored process synergies through detailed analysis, including optimizing microbial leaching conditions and the efficiency of alloy formation and grinding processes.

2. Materials and methods

Fig. 2 provides an overview of a process scheme to help readers to better understand the different process steps. As can be seen, two different approaches are compared: one combined approach of pyrometallurgy and biohydrometallurgy (Route 1) and one stand-alone biohydrometallurgical approach (Route 2), both with a synthesized black mass, according to Table 1

2.1. LIB sample preparation

The use of synthetic black mass was selected to ensure controlled and reproducible experimental conditions, enabling precise analysis of the underlying mechanisms during the pyrometallurgical treatments. While synthetic black mass closely mimics the elemental composition of real black mass derived from spent LIBs, differences in the presence of impurities such as binders and electrolytes could potentially influence the melting behavior. However, these effects can be minimized with appropriate pre-treatment steps, such as thermal processes that effectively vaporize binders and other impurities. Such pre-treatment is commonly applied in industrial processes to ensure a cleaner black mass feedstock for subsequent metallurgical treatments. While future studies using real black mass will be necessary to capture the effects of impurities and binders fully, the results from synthetic black mass trials are expected to remain relevant for comparison, particularly when pre-treatment steps align the composition and thermal properties of the feedstock. Therefore, synthetic black mass offers a reliable starting point for evaluating the proposed pyrometallurgical treatments.

To mimic the composition of black mass derived from used LIBs more accurately, analytical-grade cathode material, obtained from Gelon Energy Corp., Linyi, China, with a purity of 99.5 %, was mixed with amorphous carbon powder (purity: 99.7 %) to represent the anode. Cu powder (purity: 99.7 %) and Al powder (purity: 99.1 %) were used to represent the electrode conductor foils. Additionally, iron (Fe) powder (purity: 98.6 %) was added to the mixture, simulating scrap particles generated during mechanical pre-treatment. The chemical composition of the LFP chemistry, as well as the chemistry of the NMC811 cathode chemistry, is detailed in Table 1. Analysis of the metal composition listed in Table 1 was performed using inductively coupled plasma optical emission spectroscopy (ICP-OES), while oxygen content was theoretically determined to reconcile the total to 100 %.

Considering previous tests, the mixing ratios between cathode

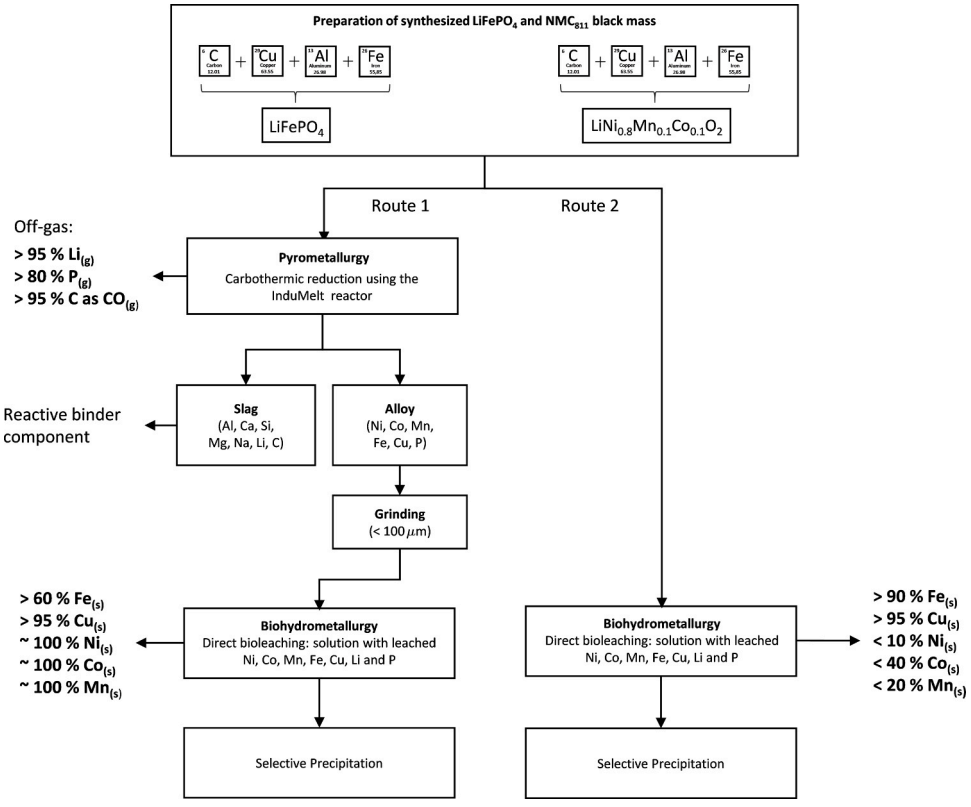

Fig. 2. Schematic overview of process steps for a combined pyro- and biohydrometallurgical way (Route 1) or a stand-alone biohydrometallurgical approach (Route 2) to recover metals from synthesized LIB black mass.

Table 1
Chemical composition of the used cathode material from production in mass percent (%).

Pure cathode material	unit	Li	Ni	Mn	Co	Fe	P	O_2
$LiFePO_4$ (LFP)	%	4.5	0.0	0.0	0.0	34.3	18.2	43.0
$LiNi_{0.8}Mn_{0.1}Co_{0.1}O_2$ (NMC811)	%	7.6	49.8	5.7	5.9	0.0	0.0	31.1

material, carbon, and other additives were done according to Wiszniewski et al. (2024) [46], where a detailed explanation of the stoichiometry and preparation is given. From that knowledge, the Cu and Fe contents in black mass from recycled batteries typically range between 1 % and 6 %, and for Al within 1 % and 3 %. Hence, an average of 3 % for Cu and Fe and 2 % for Al was assumed for the synthesized model black mass. The stoichiometric minimum requirement of carbon under consideration of process-specific conditions was determined to be around 20 %. However, considering that Al exhibits a stronger reduction potential compared to C, adding Al reduced the required carbon content to 17 % for these trials. Considering these assumptions, the following mixing ratio, as shown in Table 2, was applied to the materials used in this study.

2.2. Pyrometallurgical treatment

The pyrometallurgical treatment was performed using the batch-operated InduMelt reactor [49,50], based on the InduRed reactor concept [47,48]. A schematic overview of the InduMelt reactor is given in the graphical abstract and Appendix B (Figure B1). This inductively heated system utilizes a packed bed of graphite cubes as a susceptor, converting electromagnetic energy into heat via ohmic resistance. A copper induction coil encircling the crucible generates the required heat to sustain the reaction temperature, with a maximum power output of 7.5 kW. This coil induces an eddy current in the graphite cubes, which heats them through their inherent ohmic resistance. By using renewable energies, this reactor can substantially reduce the overall environmental impact of pyrometallurgy and act as an ecological alternative in future pyrometallurgical recycling approaches.

The fine black mass input is distributed between layers of graphite cubes within a ceramic crucible, where additional carbon serves as a reducing agent to facilitate carbothermic reduction while minimizing wear on the graphite cubes' structure. The reactor reaches temperatures of up to 1500 °C, enabling the effective evaporation of volatile elements such as lithium and phosphorus via the gas phase. Off-gas is collected through an alumina off-gas pipe and washed to recover volatile components. A detailed description of the apparatus setup is given in previous studies conducted by Holzer et al. [50], with further improvements implemented and described in Wiszniewski et al. [46].

Approximately 24 hours post-heating phase, once the crucible and its contents had cooled to ambient temperature, the graphite cubes and solid fractions—comprising a metal alloy, magnetic powder, and non-magnetic powder (slag)—were extracted and separated using sieving (up to a particle size of 0.5 mm) and magnetic separation with a neodymium bar magnet. The alloy was crushed using a jaw crusher equipped with titanium jaws (Retsch BB 200 WC) to remove sintered products that adhered to its surface effectively. After crushing, the material was subjected to sieving and magnetic separation to isolate the pure alloy fraction. Only this purified alloy fraction was subsequently grinded to achieve the target particle size required for biohydrometallurgical leaching. Since Li is not bound within the matrix of the slag phase using this pyrometallurgical approach, the slag phase is not investigated further in this study.

Table 2
Chemical composition of the used cathode material from production in mass percent (%).

unit	Oxidic		Additive (elemental)			
	Cathode material		C	Fe	Cu	Al
%	LFP	75	17	3	3	2
%	NMC811	75	17	3	3	2

While batch-based systems often result in prolonged processing times and high energy consumption, a continuously operated reactor significantly improves time efficiency and energy utilization. This improvement is primarily due to fine powdery black mass as the input material, which melts immediately upon contact with the hot graphite bed. Furthermore, the skin effect results in heat being generated directly at the surface of the graphite cubes. Which further minimizes the overall energy demand [51]. This mechanism significantly reduces the energy required for the melting process compared to conventional heating methods. Compared to the Wöhler process, the InduRed reactor offers a more uniform temperature distribution, significantly enhancing the evaporation of lithium and phosphorus, thereby improving recovery rates [52]. While exact economic data concerning the energy input cannot be given yet, the authors plan a techno economic analysis (TEA) to combine different technologies for future research. Additionally, the continuous operation eliminates the need for cooling periods typically necessary in batch reactors, thereby reducing overall processing time and improving the system's efficiency [53].

2.3. Alloy post-treatment for desired particle size

For efficient biohydrometallurgical treatment of the alloys obtained from the InduMelt plant, achieving small particle sizes is crucial for lab experiments. A particle size below 100 μm was aimed for, as smaller particle sizes enhance the activity and reaction surface area, facilitating more efficient leaching processes and maximizing metal recovery rates while reducing the processing time [54]. Therefore, attention to grinding techniques is essential to successfully implement biohydrometallurgical treatments for the LFP and NMC811 alloy.

A ball mill was tested for grinding for the alloy resulting from the trial with LFP as input material. Parameters such as milling time, rotational speed, and ball-to-powder ratio play pivotal roles in determining the final particle size of the metal. Longer milling times and higher rotational speeds tend to produce finer particles. Still, excessive energy input can lead to undesired phase transitions, especially when in contact with oxygen from the atmosphere. To achieve the desired particle size, a milling time of 12 h was applied, with about 75 – 100 revolutions per minute (rpm). The milling vessel, made of aluminum-oxide (Al_2O_3), had an inner diameter of 160 mm and a length of 200 mm. As grinding material, zirconia-oxide balls with a diameter of 20 mm were used, where the ball-to-powder ratio was 15:1. Due to the relatively low rotational speed and resulting lower energy input, no inert atmosphere was applied.

Unlike LFP, the NMC811 alloy presents challenges in conventional ball milling due to its high ductility and tendency to deform under mechanical stress. When traditional methods such as ball milling or other grinding methods prove ineffective or impractical for particle size reduction of highly ductile materials like NMC811, mechanical filing emerges as a pragmatic alternative for lab trials. Before filing, the surface of the NMC811 alloy, as well as of the file, was cleaned and decreased to remove any contaminants that may compromise the filing process or introduce impurities. Throughout the filing process, the surface quality was periodically assessed using visual inspection to monitor particle size reduction progress and identify any irregularities or defects. Following mechanical filing, the particle size of the NMC811 alloy was classified into three samples, one higher than 250 μm with large flakes of

the alloy up to 500 μm, one lower than 250 μm and one lower than 100 μm. Only the latter two samples (< 250 μm, < 100 μm) were used for the biohydrometallurgical leaching trials.

2.4. Bioleaching

Bioleaching consortia used in the present study comprised an enriched culture dominated by *Acidithiobacillus thiooxidans* and *Alicyclobacillus disulfidooxidans*. The enrichment and adaptation process, along with the complete metagenomic results, can be found in a previous work conducted by co-authors [55]. The cultures were pre-cultivated in sterilized 100 mL Erlenmeyer flasks sealed with a cellulose stopper for 7 days in a basal salt medium as described by Ňancucheo et al. [56], 2016 with 50 millimolar (mM) of Fe^{2+} and 1 % (w/v) of elemental S added, at pH 2 and a working volume of 50 mL. After the pre-cultivation, two different test series, one with 1 % and one with 10 % (w/v) of the substrate (LFP or NMC811), were added, and the bioleaching experiment was further continued for 7 days. For the substrate, synthetic LFP (<50 μm) and NMC811 (<100 μm) after treatment in the InduMelt reactor (Section 2.2) and grinding process (Section 2.3), along with the non-treated black mass, were each tested separately. 1 mL samples were taken at regular intervals, followed by the addition of 1 mL of fresh medium to compensate for the loss in volume. Optical density (OD), pH, and oxidation-reduction potential (ORP) in millivolt (mV) were monitored during the experiment. All samples were filtered using polyamide filters (0.20 μm) and then stored at −20 °C. A chemical, abiotic control containing only the medium adjusted to the same pH (using 95 % H_2SO_4) compared to the pre-cultivation was also run in parallel with the biotic experiments. All bioleaching experiments were performed in duplicates with a shaking speed of 150 rpm and at 30 °C, which is the optimum growth temperature of mesophilic acidophile such as *A. thiooxidans*.

2.5. Selective precipitation

Selective precipitation of the leachates obtained from the biotic leaching of 10 % (w/v) NMC811 alloy was performed in triplicate. Before adjusting the pH stepwise to pH 8, 9, and 10, metal burden solutions obtained from leaching NMC811 alloys with < 100 μm and < 250 μm particle size were filtrated and merged into a single sample. pH values were determined using a laboratory pH Meter control (Knick Elektronische Messgeräte GmbH & Co. KG, Berlin, Germany). During pH adjustment with a 2 molar (M) sodium hydroxide, the leaching solution was stirred at 500 rpm using an IKA RCT basic (Staufen, Germany). After precipitation the suspension was centrifuged with a Rotina 380 centrifuge (Andreas Hettich GmbH & Co. KG, Tuttlingen, Germany) at 3000 rpm for 8 minutes. The obtained supernatant was sampled, and metal concentrations of filtered samples (0.22 μm) were determined by ICP-MS analysis. Subsequently, the remaining supernatant was used for the next pH increment step and precipitation and centrifugation followed. Furthermore, metal precipitation from LFP leachate was conducted similarly, but the pH was increased stepwise to pH 2, 3, 4, 5, and 6. Before conducting precipitation of LFP leachate, H_2O_2 was added stoichiometrically to oxidize Fe^{2+} ions into Fe^{3+} ions, as precipitation of Fe(III) is known to occur at around pH 3, whereas Fe(II) precipitates later at pH 7–8.

2.6. Analytical methods

Samples of the metallic and non-metallic fractions after pyrometallurgical treatment and the grinding process were analyzed for their chemical composition using Inductively Coupled Plasma Optical Emission Spectroscopy (ICP-OES). Samples were digested using the aqua regia method (ÖNORM EN 13657–2002) for subsequent ICP-OES analysis according to ÖNORM EN ISO 11885:2009. In this process, 3 g of the sample was treated with 60 mL of aqua regia (a 3:1 mixture of HCl 37 % and HNO_3 65 %) and refluxed at 300°C for at least 2 hours in a sealed vessel with an absorption device. After cooling, the solution was filtered through a white-band filter to remove particulates and diluted to a final volume of 250 mL.

To identify potential phases, X-ray diffraction (XRD) measurements were conducted. A Bruker D8 Advance diffractometer operating in Bragg-Brentano geometry with Cu Kα radiation (λ = 0.15418 nm) at 25 mA and 40 kV was used. Diffraction patterns were collected over a 2θ range from 10° to 100° with a step size of 0.02° and an acquisition time of 2 s per step. The XRD patterns were analyzed using SIeve+ software with the PDF-5 + 2024 database (ICDD, USA).

Sample cross-sections were examined using a Zeiss EVO MA 15 scanning electron microscope (SEM) operated with a tungsten filament at 10 kV both in backscattered electron (BSE) and secondary electron (SE) mode. Energy-dispersive X-ray (EDX) analysis was performed with an Oxford Instruments Inca DryCool EDS detector.

For optical investigations of the grinded and filed alloys, a Keyence VHX-970F digital microscope was used to detect possible irregularities in the powders. Particle size distribution of powders was obtained by means of laser diffraction using a particle sizer from CILAS 1064, Orleans, France.

The bioleaching experiment was performed in a Multitron Pro shaker (Infors HT, Switzerland). For monitoring the growth of the cultures, the OD was measured at 660 nanometer (nm) (DR3900 Hach Lange, Austria) after the samples were centrifuged at 1500 g for 1 min (5427 R Eppendorf, Germany) to separate the suspended sulfur from the cells. For measurements of pH and ORP, LE422 and Inlab Redox (vs Ag/AgCl; Mettler Toledo, Switzerland), connected to S220 pH/ion meter (Mettler Toledo, Switzerland) were used. Total Fe and Fe^{2+} concentrations were measured using ferrozine solution as an indicator, $HONH_2$-HCl as a reducing agent and $NH_4CH_3CO_2$ as a buffer solution. The measurement was done at 562 nm on a 96-well plate using an Infinite 200 Pro M Plex Microplate Reader (Tecan, Switzerland). Metal concentrations of liquid samples from bioleaching and selective precipitation were measured using Inductively Coupled Plasma Mass Spectrometry (ICP-MS) according to the ÖNORM EN ISO 17294–2:2017–01 standard. After bioleaching, the solid residue was analyzed using SEM (TM 3030, Hitachi, Japan) with an Energy Dispersive Spectroscopy (EDS) detector.

Bioleaching efficiency (E_{AC}) of each metal (and P) is calculated by using Formula 2,

$$E_{AC}(\%) = \frac{(c_L - c_M)}{c_s} \times 100 \quad (2)$$

where C_L→ concentration in the leachate solution, C_M→ concentration in the cultivation medium, and C_S → concentration in the substrate (all in mg/L). Due to the inhomogeneity of the substrate, some of the leaching efficiencies were above 100 %. For this reason, normalization according to the highest leaching efficiency which is above 100 % was done for each metal (and P).

$$\textit{normalised leaching efficiency}(\%) \quad = \frac{E_{AC}}{E_H} \times 100 \quad (3)$$

Where E_{AC}→ leaching efficiency from formula 2, E_H = highest leaching efficiency above 100 %

3. Results and discussion

3.1. Pyrometallurgical treatment within the InduMelt reactor

For each trial within the InduMelt reactor, 400 g of the mixtures listed in Table 2 were used. The fractions obtained from the experimental setup are summarized in Table 3 and were categorized based on their characteristic material properties as follows:

- Reduced and magnetic alloy

Table 3
Mass fractions of input material and products (metal, powder magnetic, and powder sparse magnetic) after pyrometallurgical treatment within the InduMelt plant in gram (g).

Sample	unit	Input	Metal	Powder magnetic	Powder sparse magnetic (slag)
LFP	g	400	140.10	6.93	40.95
NMC811	g	400	204.97	7.23	3.46

Table 4
Oxidation rates in mass percent (%) of specific elements of the NMC811 alloy based on oxygen amount as percent of input material in mass % (%).

unit	Oxygen	Al	Mn	Fe	Co	Ni
%	0.050	100.00	98.55	10.12	1.40	0.11
%	0.060	100.00	99.85	59.95	10.16	1.00
%	0.075	100.00	99.95	83.21	25.36	3.90
%	0.100	100.00	99.98	93.73	48.78	12.36

- Powder: Magnetic (particle size < 1 mm)
- Powder: Sparse magnetic (particle size < 1 mm)
- Dissolved species in the gas wash bottle

While the last listed fraction was attributed to the gas line, the first three fractions were isolated from the reactor interior.

While the conversion rate within the NMC811 mixture was sufficient, with only about 2.6 % remaining powder content regarding the overall input material, this was not the case for the LFP mixture. Rather than having a pure molten metallic fraction, a higher quantity of the powder fraction appeared. As the main focus is on the metallic fraction within this study, representative samples after pyrometallurgical treatment are only shown from the metallic alloy in Appendix B, Figure B2. In Wiszniewski et al. (2023) a graphical visualization of the different solid factions is given [57].

To investigate the phase composition and to define possible further refining steps before grinding, SEM-EDX analyses can provide the necessary information regarding the phase composition. As shown in Figure a, the LFP material primarily consists of different iron phosphides, where Fe_2P is the most dominant phase. This aligns very well with findings in recent studies conducted by the author [58], investigating the kinetics and phase evolution during carbothermic reduction of LFP, suggesting Fe_2P as the most stable iron phosphide at temperatures above 1500 °C, also supported by literature by Schlesinger [59]. Darker phases within the matrix of Fe_2P consist of Fe_3P. This matrix is interrupted by particles of smaller sizes of FeP embedded within Cu_3P. While the solid fraction is very homogenous within the whole cross-section of the alloy sample, the material's surface consists of iron-copper-oxides, where the corresponding EDX point analyses are given in Table B1 in Appendix B. Similarly, the NMC alloy in Figure c is even more homogenous, consisting of an FCC-Ni alloy, with up to 66.9 % of Ni. The surface of the metallic droplets is again covered with an oxidic layer up to a width of 10 μm consisting of manganese oxide (MnO) (Fig. 3d).

As seen within Figure c and validated via EDX point analysis, numerous inclusions of Alabandite (α-MnS) were observed within the FCC-Ni alloy, indicating the formation of stable manganese sulfide. Notably, no other sulfides were detected. This observation is crucial for the recycling process, as an alloy devoid of manganese is desirable for open-loop recycling and reuse in secondary metallurgy. As removing Mn is crucial for open-loop treatment, two theoretical options are provided:

Table 5
ICP-OES results from the different alloy powders after mechanical treatment in mass percent (%).

Material	unit	Li	Al	P	Mn	Fe	Co	Ni	Cu
LFP_P	%	0.17	0.19	22.01	-	68.67	-	-	5.60
NMC< 100	%	0.01	1.94	-	8.68	6.65	9.23	66.28	5.82
NMC< 250	%	0.01	1.88	-	7.86	6.93	9.28	67.1	5.87

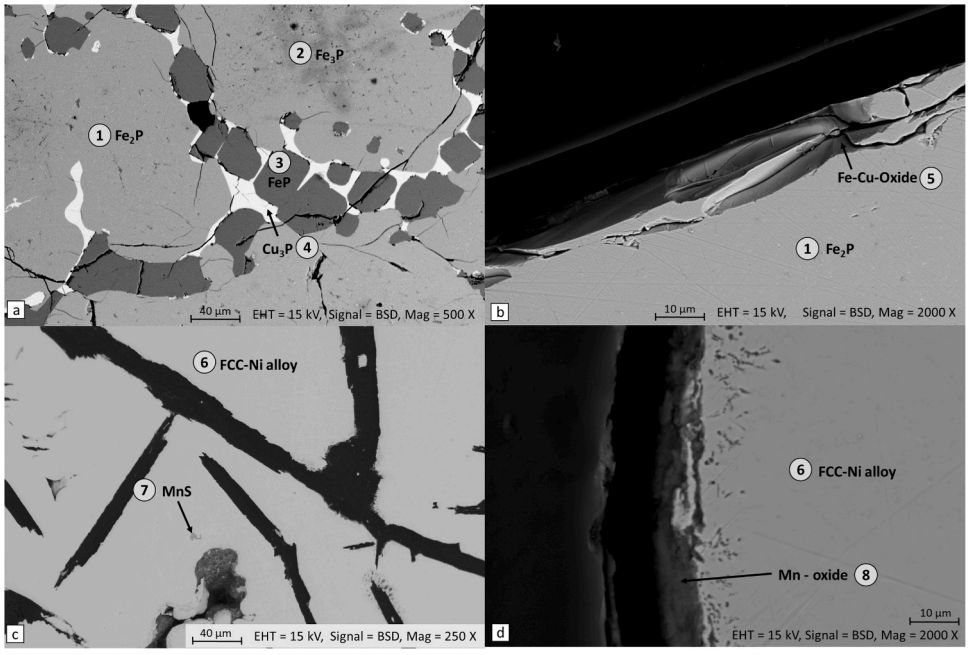

Fig. 3. SEM images with corresponding EDX point analyses of a.) LFP alloy near center, b.) LFP alloy at the surface, c.) NMC811 alloy near center, d.) NMC811 alloy at the surface with MnO layer.

The first option includes adding an appropriate amount of sulfur at elevated temperatures. As seen from the EDX results, manganese could potentially be efficiently removed from the alloy to produce high-purity MnS. This MnS can subsequently be utilized in battery production, either as high-capacity anode material [60,61] or for cathode materials [62], specifically for NMC or NMA cathodes [63]. However, for optimal use as cathode material, MnS must be converted to $MnSO_4$, which serves as a precursor material within state-of-the-art applications. The conversion of MnS to $MnSO_4$ involves oxidation, which can be achieved by reacting MnS with a strong oxidizing agent such as sulfuric acid (H_2SO_4) or hydrogen peroxide (H_2O_2), or by heating in the presence of oxygen. When sulfuric acid is used, the reaction produces $MnSO_4$, water, and hydrogen sulfide gas (H_2S), a toxic byproduct that must be handled carefully. To mitigate the release of toxic gases and avoid contaminated wastewater, oxidation at elevated temperatures is often preferred. Heating MnS in the air or an oxygen stream facilitates its conversion to $MnSO_4$ when provided as a fine powder. This reaction, however, progresses slowly at lower temperatures, necessitating higher temperatures for efficient conversion [64]. Utilizing the exhaust heat of the reactor to preheat oxygen or air can achieve these temperatures, significantly reducing CO_2 emissions within this process.

Another method to remove Mn from alloys is through partial oxidation within a controlled atmosphere. This process involves several interconnected phenomena that collectively achieve Mn removal. By adjusting the oxygen partial pressure, Mn selectively oxidizes to form MnO, which can be removed as slag. This method is particularly effective in high-temperature environments due to Mn's higher oxygen affinity than iron [65]. Internal oxidation further aids in this removal by promoting oxygen diffusion into the alloy, which reacts with Mn to form internal oxides that can be extracted [66]. Additionally, surface oxidation during processes like annealing targets Mn at the alloy's surface, refining its composition and enhancing its properties [67]. Partial oxidation of Mn from the obtained NMC alloy is furthermore calculated via the thermo-chemical Software FactSage™ 8.3 using the FactPS (2023) and SGTE alloy database (2020) shown in Figure. The calculation was performed at a constant temperature of 1600°C for an input mass of 1000 kg and a continuous oxygen addition (x-axis), whereby the temperature increase due to the exothermic character of this reaction was neglected at this first consideration.

As visualized in Fig. 4, Mn and Al removal can be achieved with almost no loss of Ni, Co, and Cu. Only if Fe is considered to be removed with high grades, partial losses of Ni and Co to the slag phase are observed. Table provides an overview of some oxygen-dependent slagging rates for each element. It can be seen that Fe can only be removed from the liquid melt alongside high losses of Co. Considering that Fe in an alloy for an open-loop approach can be accepted, the ideal amount of oxygen to obtain a product desired by the industry, lies between 50 kg and 60 kg per ton of liquid melt. For better comparability, the amount of oxygen was expressed as a relationship between oxygen amount and input material, where for example 0.05 means 50 kg oxygen per 1000 kg of input material.

While the partial oxidation of Mn requires further research especially to be validated with practical tests, the next critical step involves converting the alloy into a fine powder. Reducing the particle size is necessary to increase reactivity and dissolution rates, significantly improving the efficiency of subsequent biohydrometallurgical processes and facilitating more effective recovery and purification.

3.2. Metal grinding and powder analysis

In the previous chapter, a detailed overview of the pyrometallurgical process was given, describing the properties of the different alloys for downstream post-treatment. Following this high-temperature treatment, the alloy undergoes further processing to achieve smaller particle sizes, which is crucial for enhancing the efficiency of subsequent recycling steps, such as biohydrometallurgical treatments. Different methods were employed to achieve the desired particle size reduction based on the ductility of the alloy. For the less ductile LFP alloy, a ball mill was utilized. This method involves the use of rotating cylindrical containers filled with grinding media, which crush and grind the material into finer particles. The ball milling process successfully reduced the particle size of the LFP alloy to less than 50 μm, making it suitable for further processing. In contrast, the more ductile NMC alloy required a different approach due to its higher malleability. Filing techniques were employed to reduce the particle size of the NMC alloy. This method involves mechanically abrading the material to produce fine flakes using a shelf new file to avoid any introduction of impurities.

Microscopic examination of the powder samples provided further insights into the morphology of the processed materials (Figure). The NMC material, as observed under the microscope, consisted of flakes resulting from the filing process. These flakes indicate the mechanical abrasion technique used, which tends to produce elongated, thin particles. On the other hand, the LFP powder appeared as an agglomeration of small particles, with particle sizes ranging from less than 1 μm up to 50 μm. This agglomeration is typical of ball milling, where the grinding action produces a wide range of particle sizes, often forming clusters of fine particles.

The resulting particle size distribution for the NMC alloy was categorized into three distinct fractions using a Retsch AS 200 control sieving tower: one fraction larger than 250 μm, another between 250 and 100 μm, and a fraction smaller than 100 μm. For the subsequent biohydrometallurgical post-treatment, only the latter two fractions with 250–100 μm and smaller than 100 μm were utilized. During the determination of particle size in an aqueous solution, it was found that the LFP powder was non-magnetic, while the NMC powder was highly magnetic and floated on the surface. This finding is essential as it provides a possible solution to remove LFP chemistry from a mixed waste stream, which is especially important for biohydrometallurgical

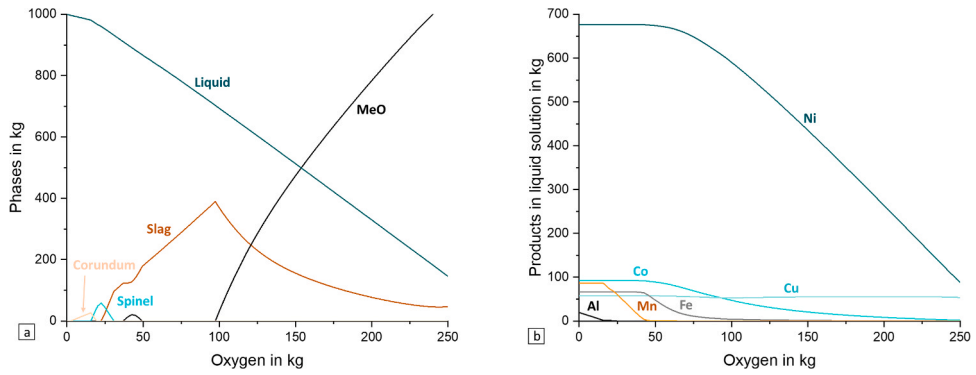

Fig. 4. Thermodynamic equilibrium calculation for partial oxidation of the NMC811 alloy using FactSage™ 8.3. a.) Overview of phases including the liquid and solid phases, b.) Overview of liquid phase dependent on oxygen amount.

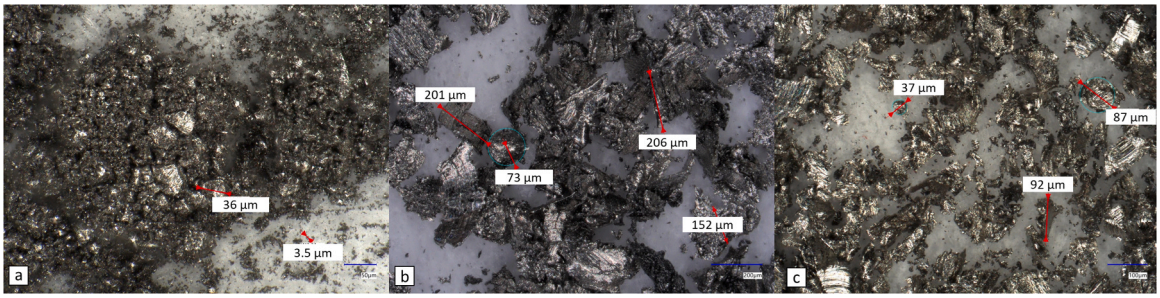

Fig. 5. Reflected light images of the alloy powders: a.) LFP powder, b.) NMC811 powder < 250 µm, c.) NMC811 powder < 100 µm.

leaching, as shown in 3.3. Consequently, a surfactant (sodium polyacrylate) was added to reduce the surface tension of the liquid, and the mixture was agitated using an ultrasonic probe to remove the particles from the surface and bring them into the liquid. The resulting particle size distribution was as follows: d_{10} / d_{50} / d_{90} = 25.3 / 76.9 / 145.7 µm.

For the LFP powder, without any pretreatment, a peak in the particle size distribution was observed around 80 µm, which contradicted the findings from the optical microscopy. This discrepancy suggested the occurrence of agglomerations. Subsequently, a dispersing agent was added (NPA-2100), and initially, agglomeration recurred over time, as seen in Figure b (V1–3 represent three different trials). However, the peak particle size was reduced to approximately 8 µm, better aligning with the microscopy results. Only after ultrasonic dispersion in combination with the dispersing agent, a relatively constant distribution, again with a peak at around 8 µm, could be achieved over time and multiple trials. This underscores the importance of potentially additional pretreatment of the powder for optimal use in hydrometallurgical processes. Although this was not further investigated within this paper, this issue could be addressed in future research work. In Fig. 6, Q3 is the volume-based cumulative curve of the particle size distribution, which states the volume percent of particles smaller than the grain size given on the x-axis, while q3 is the corresponding density function (i.e. the first derivative of Q3).

To further characterize the processed materials, an ICP-OES analysis was conducted on the three powder fractions: LFP, NMC smaller than 250 µm, and NMC smaller than 100 µm. This method was essential for determining the elemental composition of the samples, providing valuable information on the presence and concentration of various elements. The results of the ICP-OES analysis are summarized in Table, offering a detailed breakdown of the elemental composition of each fraction. Deviations from a 100 % detection rate in the ICP-OES analyses could be attributed to several factors. Oxygen and carbon, which cannot be detected via ICP, may account for some of the undetected mass. Additionally, elements other than Li and P, smaller than 0.1 % are not considered in this table and slightly affect the deviation to a 100 % detection rate. Another possibility is the presence of silicates, which cannot be dissolved with the aqua regia used in these trials, leading to incomplete dissolution and subsequent detection gaps.

While effective for small-scale lab trials, ball milling and filing are less suitable for large-scale applications due to limitations in uniformity and scalability. An alternative route, ideally fitting to a continuously operated reactor such as the InduRed, could be the atomization of the molten phases. This technique offers the advantage of processing already heated melts, where energy consumption for melting the alloy can be reduced, and simultaneously, heat recovery methods can be applied. In the continuously operated plant, the temperature and, therefore, the dynamic viscosity of the melt can be precisely adjusted for optimized atomization. Recent studies have demonstrated that not only the viscosity [68] of the metal but also the temperature and pressure [69] of the atomizing gas play crucial roles in determining the final particle size of the powders to be produced. Industrial setups leveraging these parameters can consistently produce fine, uniform metal powders. These powders are critical for advanced applications such as additive manufacturing or downstream purification techniques, including bioleaching followed by selective precipitation. However, atomization could be energy-intensive, particularly in scaling up to industrial levels. Addressing this, heat recovery systems integrated into the process can partially offset the high energy demand, making the operation more sustainable. The challenge of implementing atomization on an industrial scale involves not only energy considerations but also the design of robust, cost-effective systems capable of handling large volumes. While small-scale lab devices present inherent difficulties due to limitations in material throughput and device efficiency, the advantages of adopting atomization for industrial applications outweigh these challenges. With proper optimization, including innovations in energy recovery and atomizing nozzle design, atomization is a promising solution for high-efficiency, large-scale production of metal powders within this specific approach. Further research and pilot-scale testing will be critical to refining the balance between energy efficiency and output quality, ensuring the feasibility of implementing atomization on an industrial scale. Theoretical simulations and small-scale test series are planned for further supporting publications.

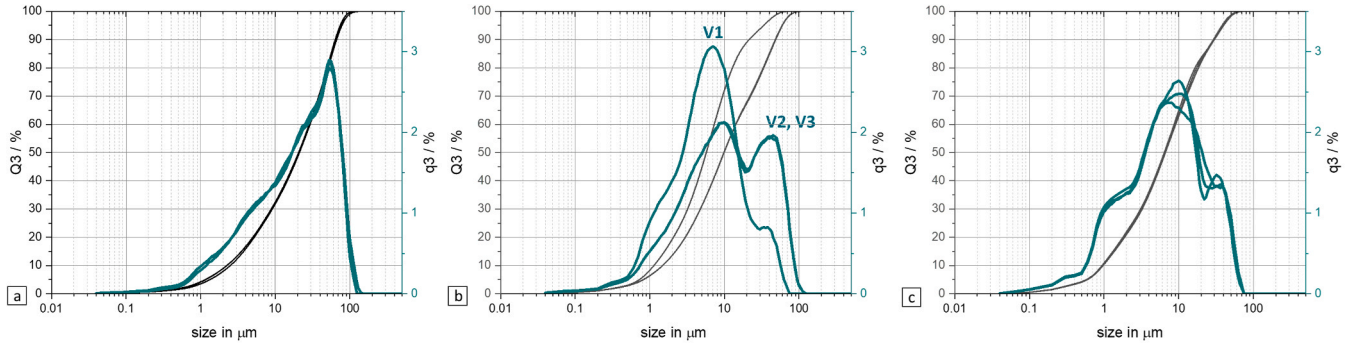

Fig. 6. Cumulative particle size distribution of the LFP powder with different pre-treatment steps: a.) no pre-treatment, b.) addition of dispersing agent (NPA-2100), c.) addition of dispersing agent (NPA-2100) and ultrasound treatment.

3.3. Bioleaching

To compare the effect of pyrometallurgical and further post-treatment of synthetic black mass (both NMC and LFP) on the metal leaching efficiency during direct bioleaching, a pulp density of both 1 % and 10 % (w/v) were tested using an adapted, enriched culture. The measurement of the leaching efficiency of the different metals and P at day 0 represents the leaching efficiency after 2 hours. The leaching efficiency was calculated using formula 2, or formula 2 with 3 if the leaching efficiency of that metal is higher than 100 %.

High leaching efficiencies of up to 100 % of Ni, Mn and Co were achieved by the enriched cultures from the 1 % treated NMC (t-NMC bio) while the untreated NMC (u-NMC_bio) has a comparatively lower leaching efficiency (<40 %) for these metals (Fig. 7a, b, c).

The poorer solubility of the untreated materials can be explained by the oxidation state of metals such as Ni, Mn, and Co, which are present as 2-, 3-, or 4-valent metal oxides in the NMC black mass and mostly in less soluble oxidation states [70]. During the pyrometallurgical treatment, the metal oxides were reduced to their metallic form representing a material easier to leach. This is one possible reason why the leaching efficiencies of these metals were higher in the treated t-NMC than in the untreated u-NMC. The cultures in the untreated NMC were able to oxidize S and hence lower the pH up to 0.7 after day 7. On the other hand, cultures in the treated NMC (t-NMC_bio) could oxidize the Fe^{2+}, indicated by the increase in Fe^{3+} concentration and ORP after day 4 (Figure B3 in Appendix B). This microbial-produced H_2SO_4 and Fe^{3+} (Eqs. 4 and 5) solubilized the metals, which resulted in the biotic experiments having higher recovery of metals than the chemical control [71]. For the treated t-NMC, the dissolution of the metals could follow Eq. 7. In contrast, for the untreated NMC, the metal oxides require reducing agents such as H_2O_2 for higher recovery as shown by Eq. 6 [72]. Therefore, in the absence of a reducing agent, the untreated u-NMC has lower leaching efficiency of Ni, Mn and Co as compared to the treated t-NMC. When the pulp density was increased to 10 %, the leaching efficiencies of Ni, Mn and Co decreased to < 20 % (Fig. 7d, e, f). This could be accredited to the alkaline nature of the NMC with increased pH (>4) and subsequent inhibition of the cultures resulted in no growth and no oxidation of S or Fe by the cultures, depicted by the low OD and Fe^{2+}/Fe^{3+} concentration respectively (Figure B4 in Appendix B). A previous study performed by Naseri et al. (2019), tested different pulp densities (1 % and 10 %) of spent coin cells during bioleaching. It revealed that the leaching efficiency of Li and Co declined from 100 % to < 70 % and < 20 % when the pulp density was increased from 1 % to 10 %, respectively [73]. Similar results were reported where the leaching efficiency decreased from 52 % to 10 % for Co and 80–37 % for Li when the pulp density was increased from 1 % to 4 % during the bioleaching experiment of spent LIB, respectively [74]

$$4Fe^{2+} + O_2 + \quad 4H^+ \rightleftharpoons 4Fe^{3+} + \quad 4H_2O \quad (microbial) \tag{4}$$

$$2S + 3O_2 + \quad 2H_2O \rightleftharpoons 2SO_4{}^{2-} + \quad 2H^+ \rightleftharpoons \quad 2H_2SO_4 \quad (microbial) \tag{5}$$

$$2LiCoO_2(s) + H_2SO_4(aq) + \quad H_2O_2(aq) \rightleftharpoons 2CoSO_4(aq) + \quad Li_2SO_4(aq) + \quad 4H_2O(g) + \quad O_2(g) \quad (chemical) \tag{6}$$

$$Co(s) + H_2SO_4 \quad \rightleftharpoons CoSO_4(aq) + \quad H_2(g) \quad (chemical) \tag{7}$$

$$2Fe^{3+} + Cu \rightleftharpoons \quad 2Fe^{2+} + \quad Cu^{2+} \quad (chemical) \tag{8}$$

During the direct bioleaching of 1 % LFP, high recovery rates of Li with > 90 % were achieved in all experiments except the chemical control (Fig. 8a, b, c). For 10 % LFP, the highest Li recovery (80 %) was obtained by the cultures from the treated (t-LFP_bio) (Fig. 8d).

Li is leached via acid dissolution in the biotic experiments (t-LFP_bio

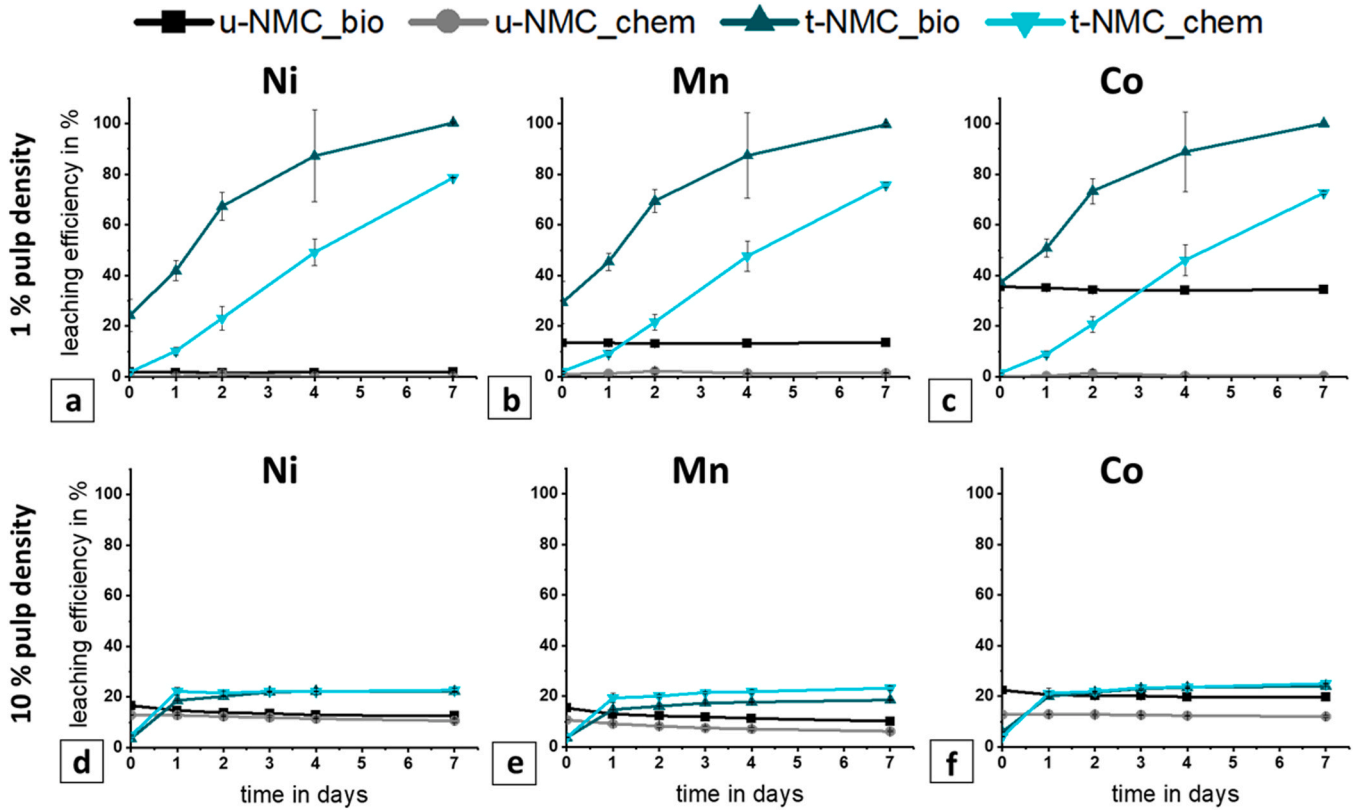

Fig. 7. Leaching efficiency of Ni, Mn and Co during bioleaching of 1 % pulp density a), b) & c) and 10 % pulp density d), e) & f), respectively, of untreated NMC (u-NMC) and treated NMC (t-NMC). Both biotic experiments using the enriched culture (bio) and a chemical control (chem) were prepared. Error bar represents standard deviation (n = 2). Day 0 is 2 hrs after addition of the black mass.

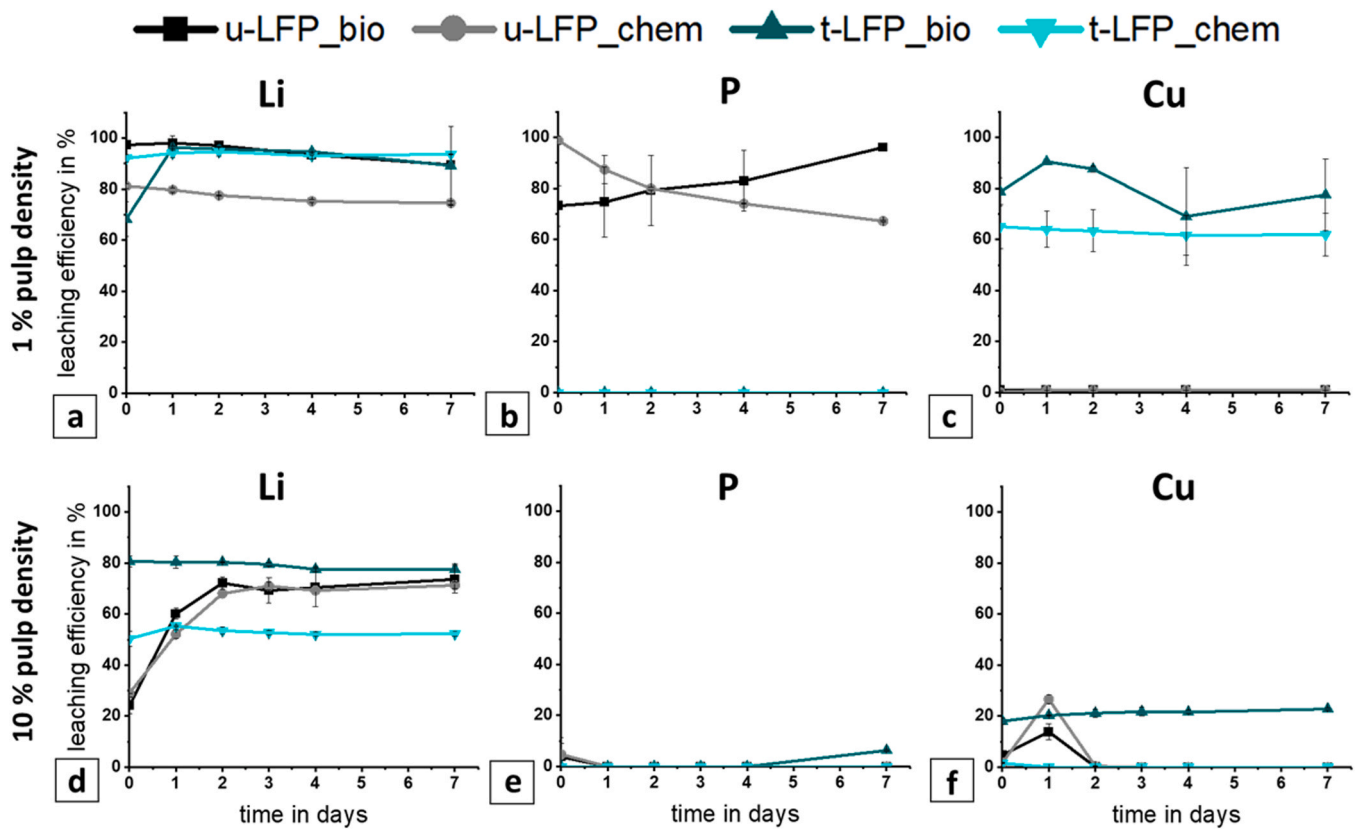

Fig. 8. Leaching efficiency of Li, P and Cu during bioleaching of 1 % pulp density a), b) & c) and 10 % pulp density d), e) & f), respectively, of untreated LFP (u-LFP) and treated NMC (t-LFP). Both biotic experiments using the enriched culture (bio) and a chemical control (chem) were prepared. Error bar represents standard deviation (n = 2). Day 0 is 2 hrs after addition of the black mass.

and u-LFP_bio), where the microbially produced H_2SO_4 plays a key role in achieving the high Li recovery rates. [75]For P, up to 100 % was leached from the untreated LFP (u-LFP_bio) but when the pulp density was increased to 10 %, little to no P was solubilized in all the experiments (Fig. 8b and e). Under acidic and reductive conditions, LFP can be decomposed to Li^+, Fe^{2+}, and H_3PO_4 using acids such as H_2SO_4. When pH and ORP are increased, $FePO_4{\cdot}2\,H_2O$ can be precipitated [76]. This could explain the low recovery of both Fe and P, suggesting that during the bioleaching experiment, the dissolution of the LFP could follow the same route and $FePO_4{\cdot}2\,H_2O$ may be formed and precipitated in both u-LFP and t-LFP experiments when pH and ORP increased (Figure B5 and B6 in Appendix B). It has been reported that Cu leaching is mainly through the Fe^{2+}/Fe^{3+} oxidation-reduction cycle (Eqs. 4 and 8) [77]. In a study by Gan et al. the mobilization rate of Cu during the bioleaching of printed circuit boards by *A. ferrooxidans* increased with the increase in Fe^{3+} concentration [78]. Clearly visible, in the treated t-LFP_bio, the microorganisms could grow (shown as an increase in OD) and metabolize Fe^{2+} (increase in Fe^{3+} concentration), thereby generating the required Fe^{3+}, which further promotes the leaching of Cu (Figure B5 in Appendix B). In contrast, in both experiments using the untreated LFP material (u-LFP_bio and u-LFPchem), the Fe concentration decreased greatly after day 1, due to the rise in pH above 4, leading to Fe precipitation (Figure B6 in Appendix B). This could explain the low recovery of Cu and other metals in the u-LFP_bio and u-LFP_chem as it has been reported that complexed metal ions co-precipitate with Fe^{3+} during the formation of Jarosite [$KFe(SO_4)_2(OH)_6$]. Additionally, the formation of Jarosite could form a passive layer on the surface of the substrate which can further prevent the dissolution of metals during bioleaching [79]. The SEM/EDS analysis of the solid residue after bioleaching with 10 % pulp density confirmed the Fe precipitation in both treated LFP and NMC and revealed the presence of unsolubilized metals such as Ni, Co, Mn and Cu in the residue (Figure B7 in Appendix B). Since the growth medium already contains added Fe^{2+}, the leaching efficiency of Fe was not included in Fig. 8.

For both LFP and NMC, the treated BM were more readily mixed in the flask as compared to the untreated ones which could be due to the hydrophobic graphite in the untreated BM. This may also be the reason why the leaching efficiency of most of the metals were better for the treated NMC and LFP. Overall, for direct bioleaching, attaining optimal pulp density is vital when comparing the results from 1 % and 10 % pulp density experiments. Maintaining a low pH is also very crucial for high metal leaching efficiency to prevent precipitation and provide ideal acidic conditions for the acidophiles. This can be done either by reducing the pulp density or by controlling the pH, adding externally, for example, biogenic H_2SO_4. As a high pulp density is the limiting factor for the direct bioleaching approach, applying indirect bioleaching for a high pulp density could be a viable option. In this method, the metabolites such as H_2SO_4 or Fe^{3+} are produced separately in a reactor using sulfur or Fe-oxidizing bacteria, and then the biogenic H_2SO_4 or Fe^{3+} is used for leaching the substrate. Indirect bioleaching has been reported to have a higher yield with less leaching time [80,81]. For NMC, the reductive pyrometallurgical treatment, which reduced the metal oxide such as Ni, Co and Mn to their metallic form, greatly improves their solubilization during bioleaching. However, for LFP the pyro-treated and the untreated have similar leaching efficiencies of metal and P, where the formation of highly stable phosphides in the pyrometallurgical step could be one reason. However, further study will be needed in order to identify the detailed mechanism.

3.3.1. *Effect of the size distribution of substrate*

As previous studies showed, the size of the substrate could also have an influence on the leachability of metals during bioleaching [54,82].

Two size fractions of treated NMC alloy - 250–100 µm (N250) and < 100 µm (N100), were tested as a substrate for direct bioleaching with 10 % (w/v). Fig. 9 shows that the leaching efficiency of metals such as Li, Ni, Mn, and Co were very similar between N100 and N250, and no significant difference was apparent. As discussed in Section 3.2, the NMC alloy is very ductile and hence causes some complications during milling and consumes more time and energy. If further milling to a smaller size could be avoided, this could have an economic advantage for further research or even up-scaling of the process and addresses the critical considerations in paragraph 3.2 regarding the atomization of the metal alloy.

3.4. Selective precipitation

After the biohydrometallurgical processing of the pretreated NMC alloy, metal precipitation from the filtrated leachate of the 10 % pulp density experiments (Chapter 3.3.2) has been investigated, by increasing the pH stepwise, from an initial pH of 6.5 up to pH 10. NMC leachates from both size distributions (N100 and N250) were combined, allowing to perform experiments in triplicate. The mixed NMC leachate had the following metal composition at pH 6.5: 15.70 g/L Ni, 2.43 g/L Co, 1.99 g/L Mn. Very low concentrations (< 100 mg/L) of Fe, Al, Cu, and Li have been measured and were therefore not displayed in Fig. 10a. The accumulated precipitation of Mn, Co and Ni at pH 8, 9 and 10 is shown in Fig. 10b. At pH 8, co-precipitation of 94 % Co and 91 % Ni was detected, and 27 % of Mn has been precipitated. However, due to a much higher share of Ni in the leachate compared to Co and Mn, a high proportion of Ni was precipitated, which led to a Ni decrease of 14.32 g/L. In comparison, Co decreased by 2.29 g/L and Mn by 0.54 g/L. Therefore, the generated precipitate was dominated by Ni precipitates. At pH 9, 100 % Co, 100 % Ni, and 48 % Mn were precipitated, and by further addition of sodium hydroxide, the pH was increased to 10, which led to 95 % Mn precipitation. Due to the previous separation of large portions of Ni and Co at pH 8, the highest share of precipitant at pH 10 accounted for Mn, leading to 0.94 g/L Mn precipitation, 0.008 g/L Co, and 0.038 g/L Ni. According to these results, precipitation at pH 10 can form a $Mn(OH)_2$ dominated precipitate with low impurities. MnO_2 is well known for its usage as a precursor for LIB production. To obtain high-purity products, several separation techniques such as precipitation (e.g. removal of impurities such as Al, Cu, Fe), solvent extraction (e.g. for Co, Ni, Mn) and (evaporative) crystallization can be applied and combined to produce battery grade Li, Ni, Mn salts [83,84]. For instance, Han and co-workers have used BaS to precipitate Co, Ni and Zn from Mn rich stripped solution to obtain battery grade $MnSO_4$ after a solvent extraction step [85]. Another possibility to remove impurities from the precipitate is acid washing, which has improved the purity of MnO_2 precipitate in a recent study above 98 % [86]. In total 259 mL/L sodium hydroxide was needed for increasing the pH from 6.5 up to 10, especially for raising the pH from 6.5 to 8, most sodium hydroxide was consumed. In a recent study 98.6 % Ni, 98.4 % Mn and 98.7 % Co have been recovered via precipitation as $Ni_{0.5}Mn_{0.3}Co_{0.2}(OH)_2$ after sulfuric acid leaching of spent Li-ion batteries by addition of Li(OH) till pH 13.05 [87]. In line with our results, at pH 8, high recovery efficiencies (>70 %) for Co and Ni have been detected and Mn has been recovered at lower levels [87]. By a further pH increase to pH 13.05 also almost the entire Mn was recovered. Based on this reference and due to experimental observations in this paper, Co and Ni precipitation from NMC leachate at pH 8 is suggested, whereas Mn could be recovered with only low Co and Ni impurities at pH 10. Error bars and standard deviations within Fig. 10 and Fig. 11 were calculated using the Excel STABWN function.

Furthermore, selective precipitation of LFP leachate, from biotic leaching experiments of pretreated LFP alloy at 10 % pulp density, was conducted in duplicate by increasing the pH stepwise from pH 1.8 up to pH 6. The initial LFP leachate at pH 1.8 had the following concentration: 7.49 g/L Fe, 1.23 g/L P and 1.57 g/L Cu as shown in Figure. Low metal concentrations of Al and Li (<0.25 g/L) have been measured and were therefore not shown in Figurea, but results have been added in the Supplementary Information. The accumulated precipitation at pH 2, 3, 4, 5 and 6 of Fe, P and Cu is depicted in Figureb. At pH 2 100 % of P co-deposited together with 82 % Fe and 36 % Cu. Adjusting to pH 2 causes the precipitation of high proportions of Fe and P and a strong decrease in Fe (5.94 g/L) and P (1.23 g/L) concentration, whereas Cu decreased moderately (0.42 g/L) as depicted in Figurea. *By further base addition till pH 3, 99 % of Fe was precipitated, whereas Cu and Li behaved rather stably and remained to an extent in solution. At pH 4 and 5 44 % and 62 % of Cu was precipitated, respectively. By further pH increase until pH 6, 91 % of Cu has been precipitated from the LFP leachate. In total, 233 mL/L of sodium hydroxide was consumed during the experiment. Especially for the first pH adjustment from pH 1.8 to pH 2, a major amount of sodium hydroxide (134 mL/L) was needed.*

According to these results, high shares of Fe and P could be recovered by adjusting the LFP leachate till pH 3, whereby only moderate Cu and low Al and Li concentrations simultaneously co-precipitated. An environmentally friendly and effective recovery of $FePO_4$ and Li from LFP batteries is urgent to prevent environmental pollution and reuse valuable materials because the production and usage of LFP batteries has significantly increased due to their advantages (e.g., safer usage and long lifespan) [88]. Moreover, regarding the EU battery regulation from 2023 80 % of Lithium should be recycled till the end of 2031 [89]. Furthermore, phosphorus was ranked as a critical raw material in the EU list of critical raw materials in 2023 [90]. However, to use the generated $FePO_4$ as a precursor for battery production a high purity is crucial. According to Feng et al. (2024) [91], optimal precipitation of $FePO_4$, in terms of recovery and purity, would be obtained at a pH of 1, however, even at such low pH, 10.3 % of Al and 1.2 % of Cu co-precipitation was reported. To recover the majority of Cu, base addition till pH 6 is necessary and an intermediate precipitation at pH 4, thus removing the remaining Fe, would support obtaining a low impurity precipitate.

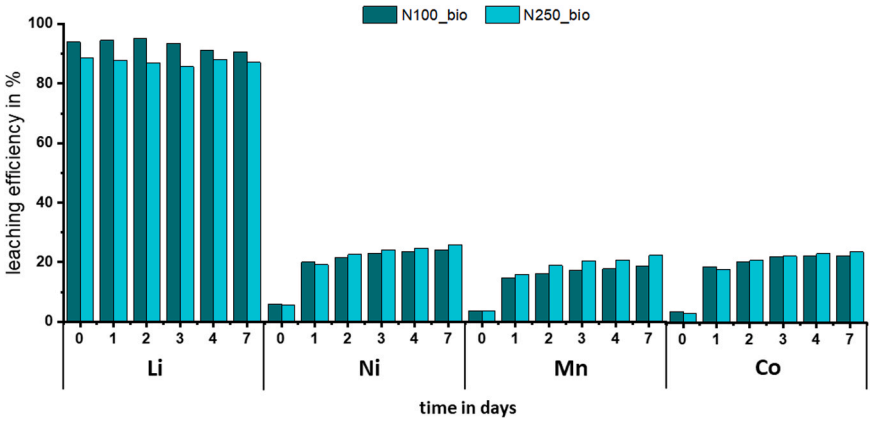

Fig. 9. Comparison of leaching efficiencies of metals between two size distributions of treated NMC, < 250 nm (N250_bio) and < 100 nm (t-NMC_bio), during direct bioleaching using adapted enriched culture.

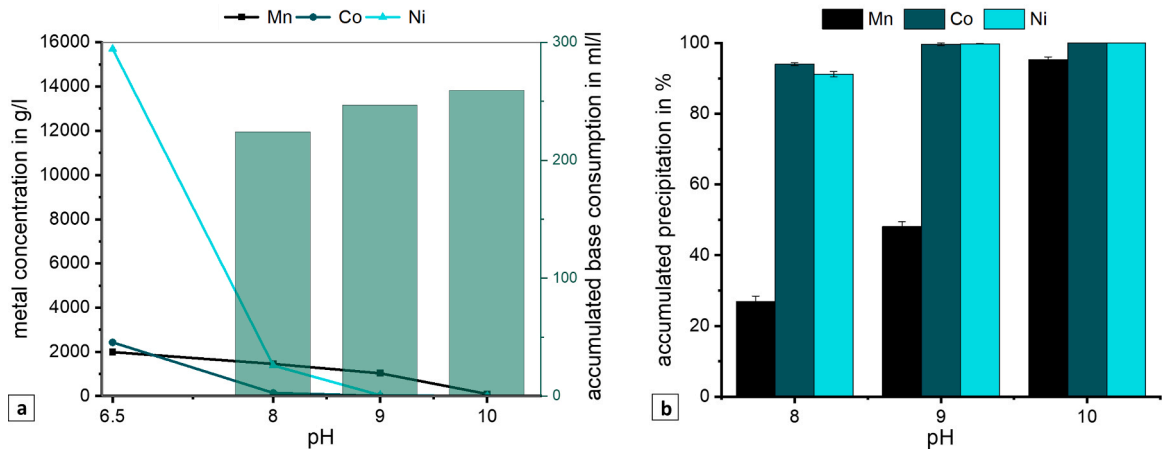

Fig. 10. a.) Metal concentrations of NMC leachate at an initial pH of 6.5 and with a stepwise pH increase from pH 8–10 together with the accumulated base consumption. Metal concentrations below 0.1 g/L are not shown. b.) Accumulated precipitation of Mn, Co and Ni from NMC leachate at pH 8, 9 and 10. Error bars indicate the standard deviation (N = 3).

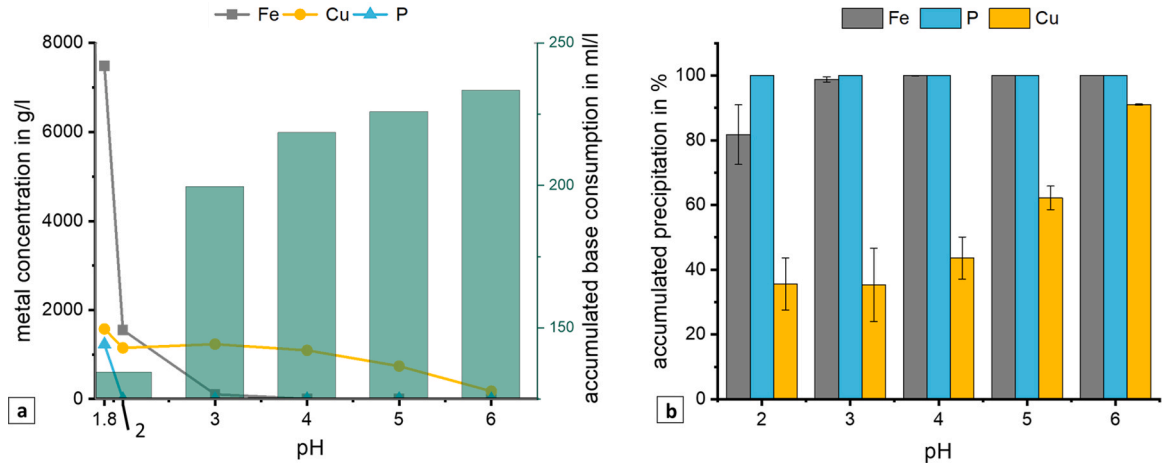

Fig. 11. a.) Metal concentrations of LFP leachate at an initial pH of 1.8 and with a stepwise pH increase from pH 2–6 together with the accumulated base consumption. b.) Accumulated precipitation of Fe, Cu, and P from LFP leachate at pH 2, 3, 4, 5, and 6. Error bars indicate the standard deviation (N = 2).

4. Conclusion – Outlook

This study investigates the potential of combining pyro- and biohydrometallurgical processes to enhance metal recovery from synthesized NMC and LFP black mass, compared to using biohydrometallurgy as a standalone approach.

Pyrometallurgical treatment was conducted using carbothermic reduction within the InduMelt reactor. Transfer coefficients of higher than 92 % for Li were achieved, leaving an almost Li-free alloy. Thermodynamic equilibrium calculations using FactSage™ indicated that partial oxidation could effectively remove remaining aluminum and manganese while minimizing losses of nickel, cobalt, iron, and copper. The optimal condition was established with 50 kg of oxygen per ton of alloy, yielding a liquid melt suitable for secondary metallurgy within an open-loop approach.

Within a closed-loop approach, the alloy was grinded to particle sizes of < 100 µm and further treated using direct biohydrometallurgical leaching with two different pulp densities(w/v) at 1 % and 10 %. The direct leaching results showed that the pyrometallurgical pre-treatment greatly improves the leachability of metals for 1 % pulp density for the untreated NMC, where up to 100 % of Ni, Mn, Co, Al, and Cu were leached in the biotic experiment. Conversely, for LFP, both pre-treated and untreated samples showed comparable leaching efficiencies, suggesting that the pre-treatment may not be as critical for this material. Therefore, for efficient recovery of NMC and other layer-structured CAMs, it is of utmost importance to remove LFP from a mixed recycling stream. The implementation of the EU's battery passport in 2027 would therefore be an economic solution to implement a proper separation between battery types.

Additionally, it was found that for Cu recovery, oxidation-reduction of Fe^{2+}/Fe^{3+} is essential. Furthermore, optimal pulp density as well as pH are critical for the direct bioleaching of both NMC and LFP to achieve a high yield. A rise in pH causes the precipitation of metals such as Fe, which can then co-precipitate with other metals or P and, therefore, lower the leaching efficiency. Precipitation of the NMC leachate showed high co-precipitation efficiencies for Co and Ni (94 % and 91 % respectively) at pH 8, whereas 95 % of Mn has been precipitated at pH 10. Precipitation results of LFP have shown that high shares of Fe and P can precipitate at pH 2, providing a potential basis for LFP precursor materials.

Overall, the results highlight that the combined approach significantly benefits the recycling of layer-structured cathode materials like NMC, while the olivine-type LFP presents challenges due to phosphide formation during pre-treatment In the biohydrometallurgical process, regulating the pH externally (using biogenic H_2SO_4) or lowering the pulp density could solve the above-described precipitation problems. Therefore, indirect bioleaching using biogenic H_2SO_4 or Fe^{3+} could be a viable option for bioleaching with high pulp densities. To reuse the

generated metals such as Ni, Co and Mn from the NMC solution, as well as Fe and P from the LFP solution, as a precursor for battery production high purity of the precipitate is crucial and needs to be further improved. However, also, an open loop reuse of the recovered Ni, Co, Fe, and P in other industrial sectors could be an interesting option and can be investigated in future research.

CRediT authorship contribution statement

Kremser Klemens: Validation, Supervision. **Doschek-Held Klaus:** Writing – review & editing, Supervision. **Guebitz Georg:** Writing – review & editing, Supervision. **Raonic Zlatko:** Writing – review & editing, Supervision. **Wiszniewski Lukas:** Writing – review & editing, Writing – original draft, Visualization, Project administration, Methodology, Investigation, Formal analysis, Conceptualization. **Lalropuia Lalropuia:** Writing – review & editing, Writing – original draft, Methodology, Investigation. **Spiess Sabine:** Writing – review & editing, Writing – original draft, Methodology, Investigation. **Presoly Peter:** Validation, Software, Investigation.

Declaration of Competing Interest

The authors declare that they have no known competing financial interests or personal relationships that could have appeared to influence the work reported in this paper.

Funding/Acknowledgement

Great thanks are owed to Andreas Egger from the chair of physical chemistry for support with SEM-EDX trials. Furthermore, huge appreciation to Emerson Barros de Souza for helping with the manual filing of metal powders. The authors gratefully acknowledge the funding support of K1-MET GmbH, the metallurgical competence center. This research received funding from the module FuLIBatteR which is supported by COMET (Competence Center for Excellent Technologies), the Austrian program for competence centers. COMET is funded by the Federal Ministry for Climate Action, Environment, Energy, Mobility, Innovation and Technology, the Federal Ministry for Labour and Economy, the Federal States of Upper Austria, and Styria as well as the Styrian Business Promotion Agency (SFG). Furthermore, Upper Austrian Research GmbH continuously supports K1-MET. Besides the public funding from COMET, the project is partially financed by the scientific partners acib GmbH, Coventry University, Montanuniversität Leoben, University of Natural Resources and Life Sciences, UVR-FIA GmbH, and the industrial partners AUDI AG, BRAIN Biotech AG, Ebner Industrieofenbau GmbH, RHI Magnesita GmbH, Saubermacher Dienstleistungs AG, TÜV SÜD Landesgesellschaft Österreich GmbH, voestalpine High Performance Metals GmbH and VTU Engineering GmbH.

Appendix A

This section is dedicated to the comprehensive description of Fig. 1, the corresponding data used, and which simplifications have been made. In 2019, the World Economic Forum (WEF) disseminated a seminal report entitled "A Vision for a Sustainable Battery Value Chain in 2030," which provides insights into the anticipated global installed battery capacity up to the year 2030. In 2023 this report was updated with a web-based statement entitled “Battery 2030: Resilient, sustainable, and circular”. Table A1 provides data from these reports.

Table A4
Global LIB battery demand in GWh for the year 2030, WEF base case

	unit	2020	2022	2025	2030
Report 2020 Total demand	GWh	282	-	971	2623
Report 2023 Total demand	GWh	-	700	1700	4700

As described in the introduction, the forecast regarding cathode chemistries also hugely changes. In Table A2 the forecasted demand from Xu et al. [8] and Pillot et al. [9] regarding shares in cathode chemistries is given.

Table A2
Share of LIB battery demand in % for the year 2030 by chemistry derived from Xu et.al (2020) and Pillot et.al (2023)

	unit	LFP	NCA	NMC	Other
Xu et al., 2020 (year 2020)	%	32.2	37.9	29.9	-
Xu et al., 2020 (year 2025)	%	20.1	40.8	39.3	-
Xu et al., 2020 (year 2030)	%	2.5	38.6	59.1	-
Pillot et al., 2023 (year 2020)	%	40.0	14.0	41.0	5.0
Pillot etal. 2023 (year 2025)	%	36.4	9.2	47.5	6.9
Pillot et al., 2023 (year 2030)	%	46.7	5.2	46.8	1.3

In Table A3, the numbers stated by the WEF scenario were then multiplied by the percentages from Xu and Pillot.

Table A3
Global LIB battery demand in GWh for the year 2030, WEF base case

	unit	LFP	NCA	NMC	Other
Xu et al., 2020 (year 2020)	GWh	90.8	106.9	84.3	-
Xu et al., 2020 (year 2025)	GWh	195.2	396.2	381.6	-
Xu et al., 2020 (year 2030)	GWh	65.6	1012.5	1550.2	-
Pillot et al., 2023 (year 2020)	GWh	280	98	287	35
Pillot et al. 2023 (year 2025)	GWh	618.8	156.4	807.5	117.3
Pillot et al., 2023 (year 2030)	GWh	2194.9	244.4	2199.6	61.1

Appendix B

This section provides an overview of additional data which supports the findings of the research.

The reactor used within this study, initially explored and well described in literature [46,49] for the recycling of sewage sludge ashes and P recovery, is for additional reader feasibility, shown in Figure B1.

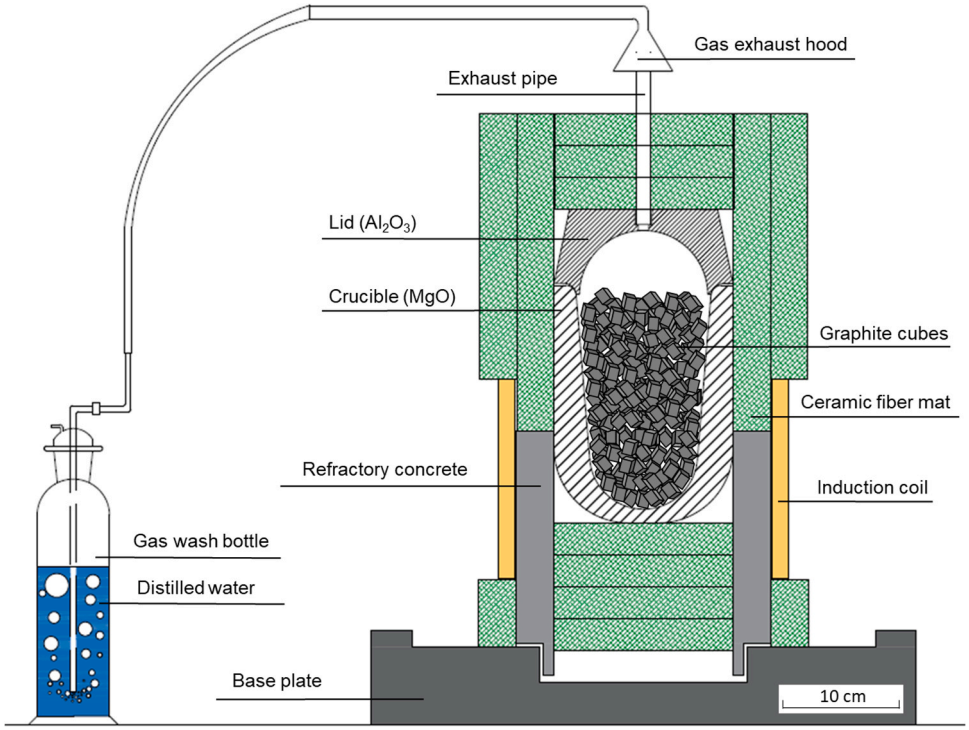

Figure B1. Schematic overview of the InduMelt reactor with gas exhaust and gas wash bottle (own depiction based on [46])

An example of the obtained alloy for both the NMC811 (Figure B2a) trial and the LFP trial (Figure B2b), after pyrometallurgical treatment within the InduMelt reactor is shown in Figure B2.

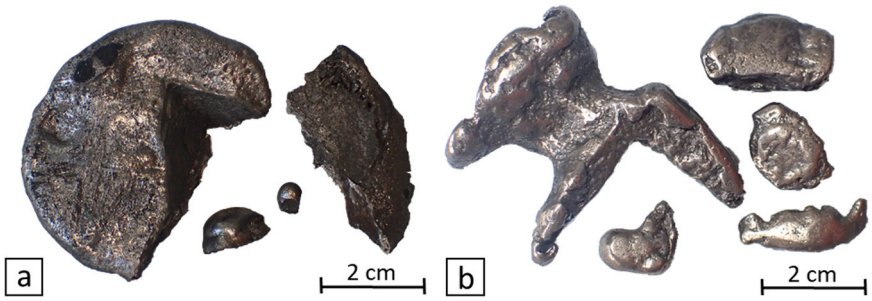

Figure B2. Representative samples of the alloy after pyrometallurgical treatment in the InduMelt reactor: a.) LFP, b.) NMC811

A SEM image of the different alloys is given in Fig. 3, where the detailed point analysis for the NMC811 alloy is given in Table B1, which shows the formation of MnS (point 7) and Mn-oxides (point 8) at the surface of the alloy.

Table B1
EDX point analyses to corresponding SEM analysis of LFP and NMC811 alloy samples in Fig. 3 in atom %

Spectrum	unit	Ni	Co	Mn	Cu	Al	Fe	P	O	S
1	atom %	-	-	-	4.2	-	66.0	29.8	-	-
2	atom %	-	-	-	5.4	-	72.1	22.5	-	-
3	atom %	-	-	-	-	-	53.8	46.2	-	-
4	atom %	-	-	-	76.0	-	1.2	22.8	-	-
5	atom %	-	-	-	9.9	-	40.4	15.4	34.3	-
6	atom %	66.9	8.8	8.4	7.0	3.2	5.7	-	-	-
7	atom %	0.8	-	46.2	2.8	-		-	-	50.2
8	atom %	1.8	4.6	36.5	-	7.1	6.0	-	43.9	-

For the bioleaching experiments additional data such as pH, OD, Fe concentration etc are given in Figures B3 to Figure B6 and are explained and

referenced to in the main text. Additionally, in Fig. 7B SEM-EDX analyses of the leached precipitates are given.

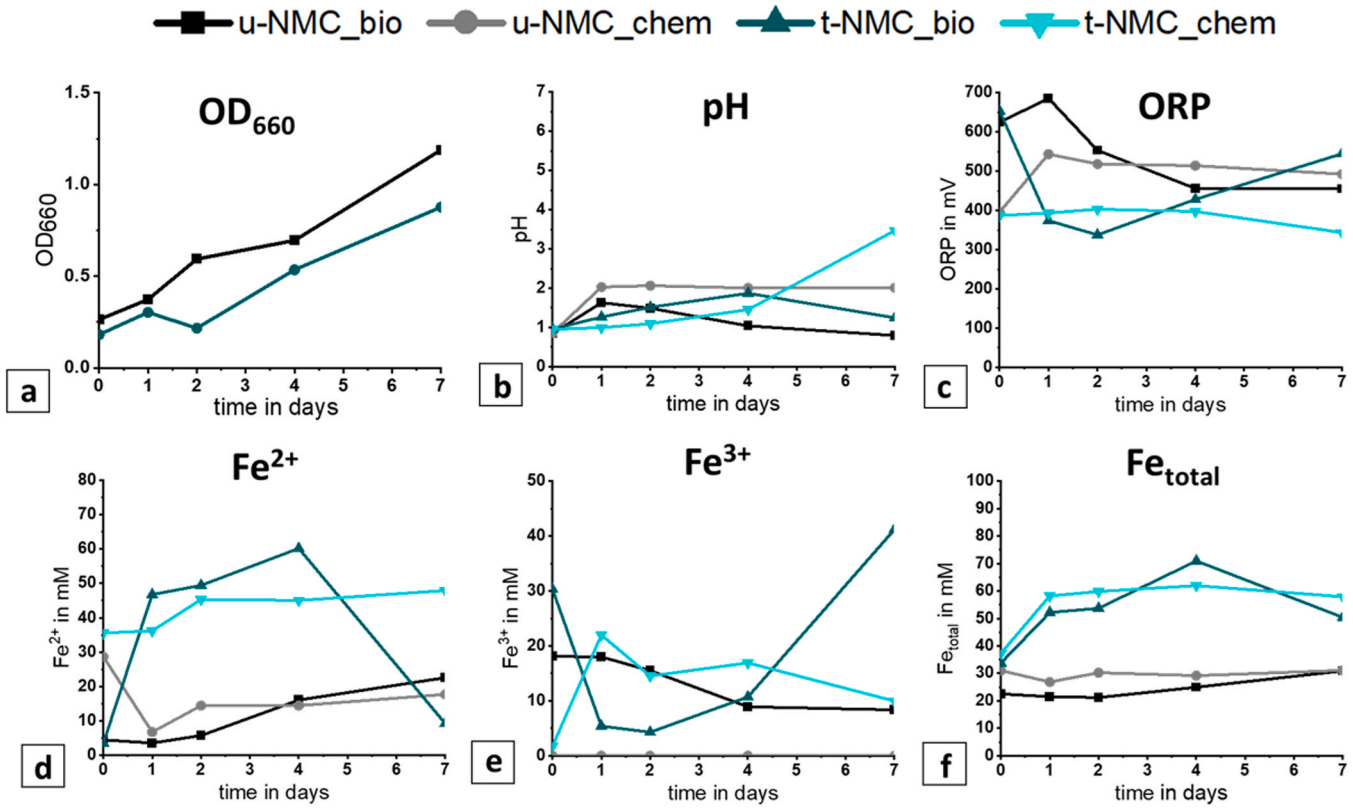

Figure B3. Measurement of a) OD_{660}, b) pH, c) ORP, d) Fe^{2+} concentration, e) Fe^{3+} concentration and f) total Fe concentration, during the course of direct bio-leaching experiment of 1 % (w/v) of both untreated NMC (u-NMC) and pyrometallurgically treated NMC (t-NMC)

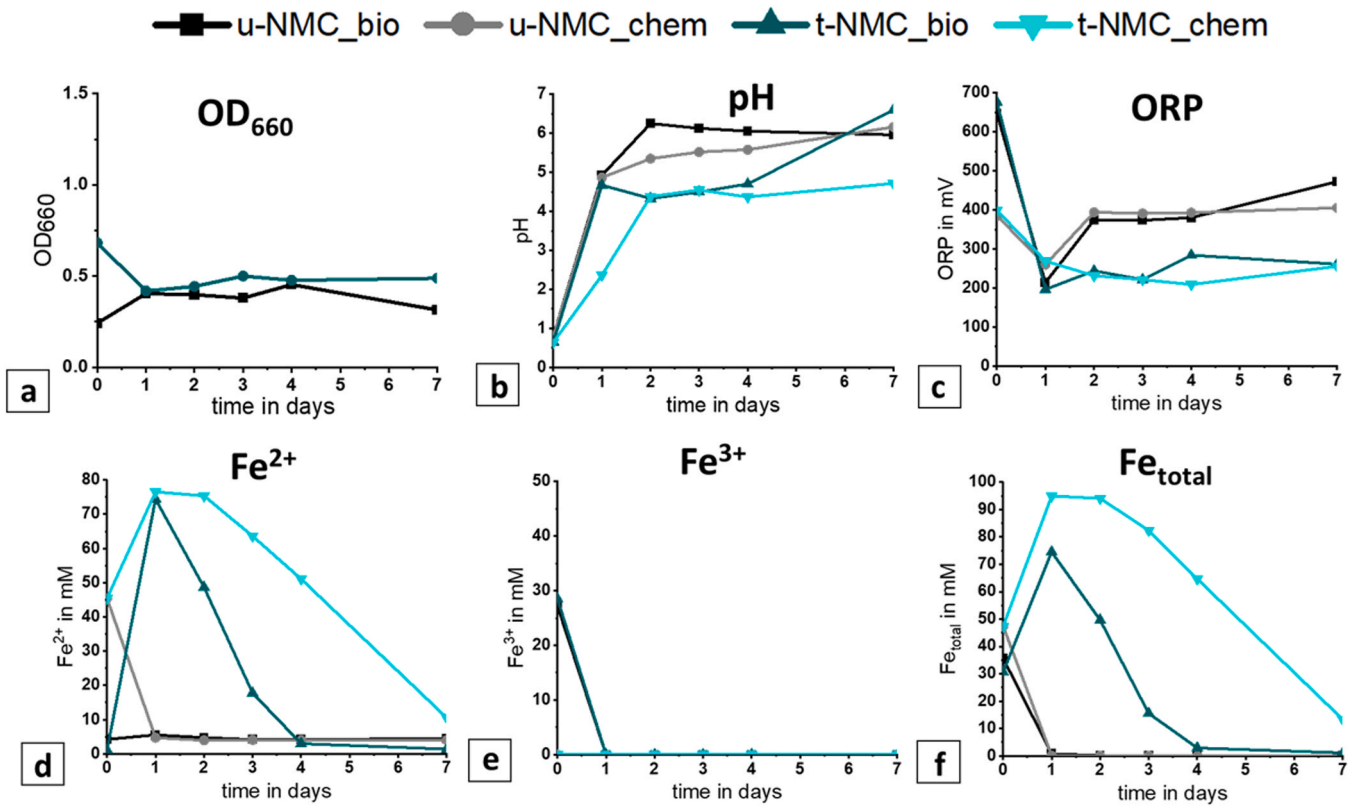

Figure B4. Measurement of a) OD_{660}, b) pH, c.) ORP, d) Fe^{2+} concentration, e) Fe^{3+} concentration and f) total Fe concentration, during the course of direct bio-leaching experiment of 10 % (w/v) of both untreated NMC (u-NMC) and pyrometallurgically treated NMC (t-NMC)

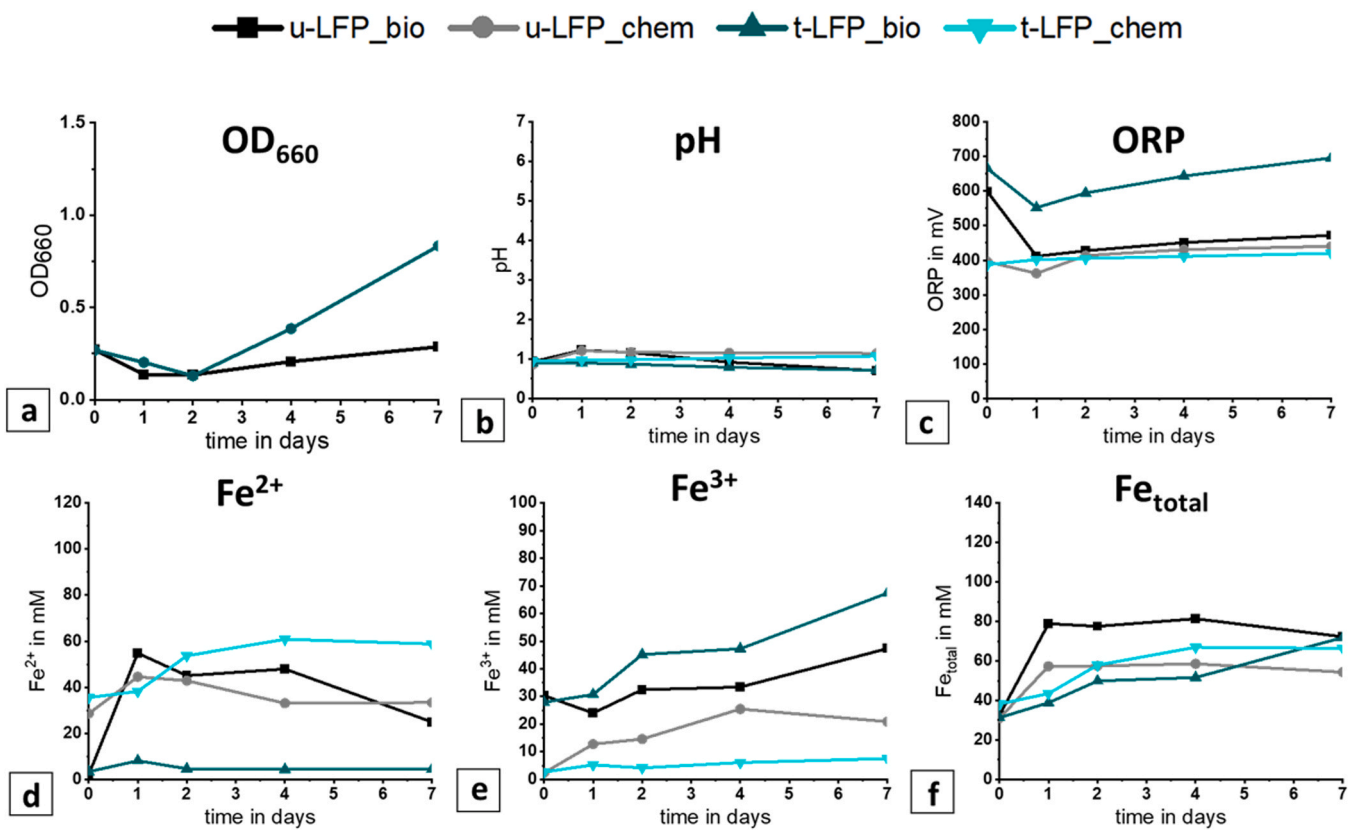

Figure B5. Measurement of a) OD_{660}, b) pH, c) ORP, d) Fe^{2+} concentration, e) Fe^{3+} concentration and f) total Fe concentration, during the course of direct bioleaching of 1 % (w/v) of both untreated LFP (u-LFP) and pyrometallurgically treated LFP (t-LFP)

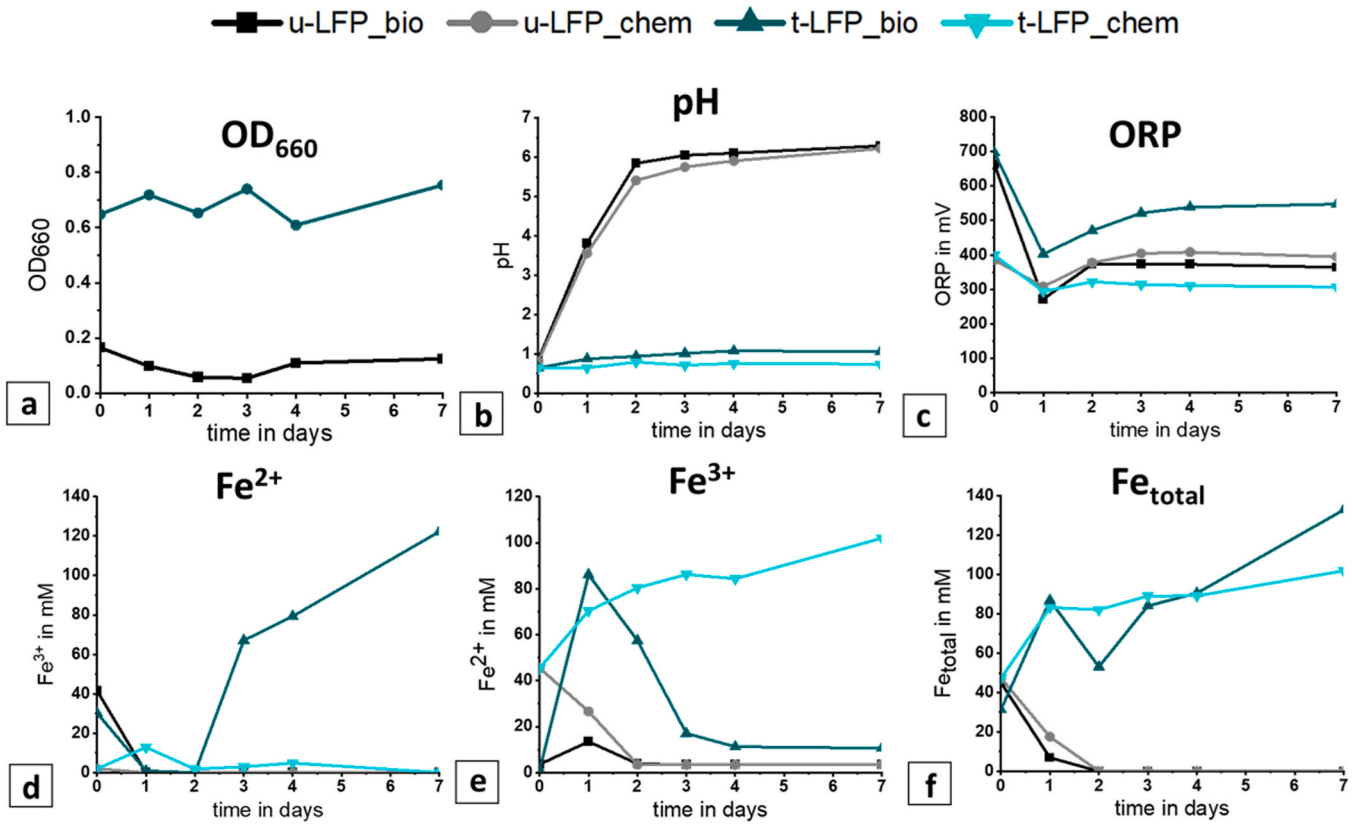

Figure B6. Measurement of a) OD_{660}, b) pH, c) ORP, d)Fe^{2+} concentration, e)Fe^{3+} concentration and f) total Fe concentration, during the course of direct bioleaching of 10 % (w/v) of both untreated LFP (u-LFP) and pyrometallurgically treated LFP (t-LFP)

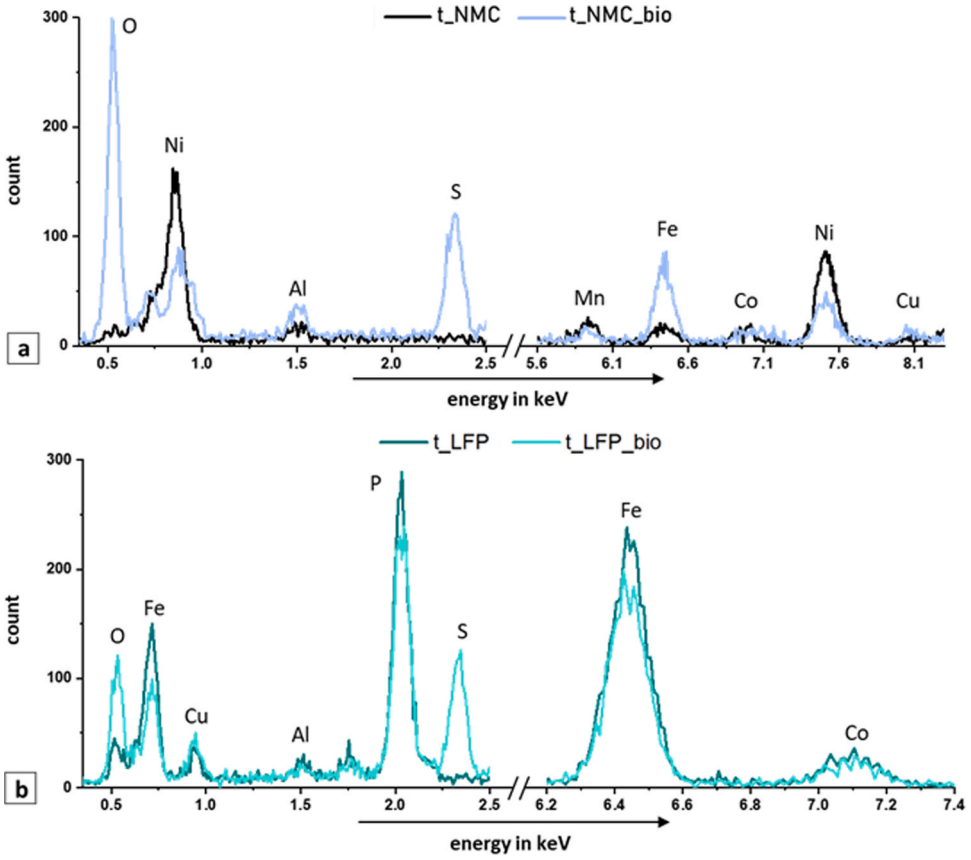

Figure B7. SEM/EDS analysis of solid residue before and after direct bioleaching of a) treated LFP (t-LFP) and b) treated NMC (t-NMC) with 10 % (w/v) pulp density using adapted enriched culture

Data Availability

Data will be made available on request.

References

[1] J. Fleischmann, M. Hanicke, E. Horetsky, D. Ibrahim, S. Jautelat, M. Linder, P. Schaufuss, L. Torscht, Alexandre van de Rijt, McKinsey & Company, 2023.

[2] Global Battery Alliance, A vision for a sustainable battery value chain in 2030: Unlocking the full potential to power sustainable development and climate change mitigation, Geneva, Switzerland, 2019.

[3] The European Parliament and the Council of the European Union, REGULATION OF THE EUROPEAN PARLIAMENT AND OF THE COUNCIL concerning batteries and waste batteries, amending Directive 2008/98/EC and Regulation (EU) 2019/1020 and repealing Directive 2006/66/EC, 2023.

[4] F. Maisel, C. Neef, F. Marscheider-Weidemann, N.F. Nissen, A forecast on future raw material demand and recycling potential of lithium-ion batteries in electric vehicles, Resour., Conserv. Recycl. 192 (2023) 106920 https://doi.org/10.1016/10.1016/j.resconrec.2023.106920.

[5] D. Kucevic, B. Tepe, S. Englberger, A. Parlikar, M. Mühlbauer, O. Bohlen, A. Jossen, H. Hesse, Standard battery energy storage system profiles: analysis of various applications for stationary energy storage systems using a holistic simulation framework, J. Energy Storage 28 (2020) 101077 https://doi.org/10.1016/10.1016/j.est.2019.101077.

[6] M. Fichtner, K. Edström, E. Ayerbe, M. Berecibar, A. Bhowmik, I.E. Castelli, S. Clark, R. Dominko, M. Erakca, A.A. Franco, A. Grimaud, B. Horstmann, A. Latz, H. Lorrmann, M. Meeus, R. Narayan, F. Pammer, J. Ruhland, H. Stein, T. Vegge, M. Weil, Rechargeable Batteries of the Future—The State of the Art from a BATTERY 2030+ Perspective, Advanced Energy Materials 12, 2102904. https://doi.org/10.1016/10.1002/aenm.202102904.

[7] S.-T. Myung, F. Maglia, K.-J. Park, C.S. Yoon, P. Lamp, S.-J. Kim, Y.-K. Sun, Nickel-rich layered cathode materials for automotive lithium-ion batteries: achievements and perspectives, ACS Energy Lett. 2 (2017) 196–223, https://doi.org/10.1016/10.1021/acsenergylett.6b00594.

[8] C. Xu, Q. Dai, L. Gaines, M. Hu, A. Tukker, B. Steubing, Future material demand for automotive lithium-based batteries, Commun. Mater. 1 (2020) 1–10, https://doi.org/10.1016/10.1038/s43246-020-00095-x.

[9] C. Pillot, Avicenne Energy. The rechargeable battery market and main trends 2022-2030, ICBR, Valencia, Spain, 2023.

[10] T. Or, S.W.D. Gourley, K. Kaliyappan, A. Yu, Z. Chen, Recycling of mixed cathode lithium-ion batteries for electric vehicles: Current status and future outlook, Carbon Energy 2 (2020) 6–43, https://doi.org/10.1016/10.1002/cey2.29.

[11] Y.E. Milian, N. Jamett, C. Cruz, S. Herrera-León, J. Chacana-Olivares, A comprehensive review of emerging technologies for recycling spent lithium-ion batteries, Sci. Total Environ. 910 (2024) 168543 https://doi.org/10.1016/10.1016/j.scitotenv.2023.168543.

[12] M. Kaya, State-of-the-art lithium-ion battery recycling technologies, Circ. Econ. 1 (2022) 100015 https://doi.org/10.1016/10.1016/j.cec.2022.100015.

[13] B. Makuza, Q. Tian, X. Guo, K. Chattopadhyay, D. Yu, Pyrometallurgical options for recycling spent lithium-ion batteries: A comprehensive review, J. Power Sources 491 (2021) 229622 https://doi.org/10.1016/10.1016/j.jpowsour.2021.229622.

[14] A. Pražanová, V. Knap, D.-I. Stroe, Lit. Rev., Recycl. Lithium-Ion.-. Batter. Electr. Veh., Part I: Recycl. Technol., Energ. 15 (2022) 1086, https://doi.org/10.1016/10.3390/en15031086.

[15] Q. Peng, X. Zhu, J. Li, Q. Liao, Y. Lai, L. Zhang, Q. Fu, X. Zhu, A novel method for carbon removal and valuable metal recovery by incorporating steam into the reduction-roasting process of spent lithium-ion batteries, Waste Manag. (N. Y., N. Y. 134 (2021) 100–109, https://doi.org/10.1016/10.1016/j.wasman.2021.08.014.

[16] J. Li, G. Wang, Z. Xu, Environmentally-friendly oxygen-free roasting/wet magnetic separation technology for in situ recycling cobalt, lithium carbonate and graphite from spent LiCoO2/graphite lithium batteries, J. Hazard. Mater. 302 (2016) 97–104, https://doi.org/10.1016/10.1016/j.jhazmat.2015.09.050.

[17] C. Pan, Y. Shen, Pyrometallurgical recycling of spent lithium-ion batteries from conventional roasting to synergistic pyrolysis with organic wastes, J. Energy Chem. 85 (2023) 547–561, https://doi.org/10.1016/10.1016/j.jechem.2023.06.040.

[18] D. Cheret, S. Santen (Umicore (B.E.)) U.S. 7,169,206 B2, 2007.

[19] S. Brouwer, J. Heulens, D. Van Horebeek W.O. 2015/096945.

[20] K. Davis, G.P. Demopoulos, Hydrometallurgical recycling technologies for NMC Li-ion battery cathodes: current industrial practice and new R&D trends, RSC Sustain 1 (2023) 1932–1951, https://doi.org/10.1016/10.1039/D3SU00142C.

[21] S. Kim, J. Bang, J. Yoo, Y. Shin, J. Bae, J. Jeong, K. Kim, P. Dong, K. Kwon, A comprehensive review on the pretreatment process in lithium-ion battery recycling, J. Clean. Prod. 294 (2021) 126329 https://doi.org/10.1016/10.1016/j.jclepro.2021.126329.

[22] X. Zeng, J. Li, B. Shen, Novel approach to recover cobalt and lithium from spent lithium-ion battery using oxalic acid, J. Hazard. Mater. 295 (2015) 112–118, https://doi.org/10.1016/10.1016/j.jhazmat.2015.02.064.
[23] H. Chen, S. Gu, Y. Guo, X. Dai, L. Zeng, K. Wang, C. He, G. Dodbiba, Y. Wei, T. Fujita, Leaching of cathode materials from spent lithium-ion batteries by using a mixture of ascorbic acid and HNO3, Hydrometallurgy 205 (2021) 105746 https://doi.org/10.1016/10.1016/j.hydromet.2021.105746.
[24] M.A.H. Shuva, A.S.W. Kurny, Dissolution Kinetics of Cathode of Spent Lithium Ion Battery in Hydrochloric Acid Solutions, J. Inst. Eng. India Ser. D. 94 (2013) 13–16, https://doi.org/10.1016/10.1007/s40033-013-0018-0.
[25] S. Virolainen, T. Wesselborg, A. Kaukinen, T. Sainio, Removal of iron, aluminium, manganese and copper from leach solutions of lithium-ion battery waste using ion exchange, Hydrometallurgy 202 (2021) 105602 https://doi.org/10.1016/10.1016/j.hydromet.2021.105602.
[26] P. Jenis, T. Zhang, B. Ramasubramanian, S. Lin, P.R. Rayavarapu, J. Yu, S. Ramakrishna, Recent progress and hurdles in cathode recycling for Li-ion batteries, Circ. Econ. 3 (2024) 100087 https://doi.org/10.1016/10.1016/j.cec.2024.100087.
[27] H. Ciftci, A. Akcil, Effect of biooxidation conditions on cyanide consumption and gold recovery from a refractory gold concentrate, Hydrometallurgy 104 (2010) 142–149, https://doi.org/10.1016/10.1016/j.hydromet.2010.05.010.
[28] A.H. Kaksonen, N.J. Boxall, Y. Gumulya, H.N. Khaleque, C. Morris, T. Bohu, K. Y. Cheng, K.M. Usher, A.-M. Lakaniemi, Recent progress in biohydrometallurgy and microbial characterisation, Hydrometallurgy 180 (2018) 7–25, https://doi.org/10.1016/10.1016/j.hydromet.2018.06.018.
[29] H.R. Watling, The bioleaching of sulphide minerals with emphasis on copper sulphides — A review, Hydrometallurgy 84 (2006) 81–108, https://doi.org/10.1016/10.1016/j.hydromet.2006.05.001.
[30] A. Schippers, S. Hedrich, J. Vasters, M. Drobe, W. Sand, S. Willscher, Biomining: metal recovery from ores with microorganisms, Adv. Biochem. Eng. /Biotechnol. 141 (2014) 1–47, https://doi.org/10.1016/10.1007/10_2013_216.
[31] M. Hong, W. Wang, L. Li, Y. Liu, L. Tong, G. Qiu, B. Yang, J. Wang, The use of biogenic Fe3+ and H2SO4 generated from pyrite waste to enhance bornite bioleaching: A potential utilization of acid mine drainage, Miner. Eng. 190 (2022) 107927 https://doi.org/10.1016/10.1016/j.mineng.2022.107927.
[32] O. Velgosová, J. Kaduková, R. Marcinčáková, P. Palfy, J. Trpčevská, Influence of H2SO4 and ferric iron on Cd bioleaching from spent Ni-Cd batteries, Waste Manag. (N. Y., N. Y.) 33 (2013) 456–461, https://doi.org/10.1016/10.1016/j.wasman.2012.10.007.
[33] K. Kremser, S. Thallner, D. Strbik, S. Spiess, J. Kucera, T. Vaculovic, D. Vsiansky, M. Haberbauer, M. Mandl, G.M. Guebitz, Leachability of metals from waste incineration residues by iron- and sulfur-oxidizing bacteria, J. Environ. Manag. 280 (2021) 111734 https://doi.org/10.1016/10.1016/j.jenvman.2020.111734.
[34] Y. Xin, X. Guo, S. Chen, J. Wang, F. Wu, B. Xin, Bioleaching of valuable metals Li, Co, Ni and Mn from spent electric vehicle Li-ion batteries for the purpose of recovery, J. Clean. Prod. 116 (2016) 249–258, https://doi.org/10.1016/10.1016/j.jclepro.2016.01.001.
[35] M. Valix, Bioleaching of Electronic Waste: Milestones and Challenges, in: J.W.-C. Wong, R.D. Tyagi, A. Pandey (Eds, in: Current developments in biotechnology and bioengineering, 18, Elsevier, AMSTERDAM, 2016, pp. 407–442.
[36] Z. Xing, M. Srinivasan, Electrochemical approach for lithium recovery from spent lithium-ion batteries: opportunities and challenges, ACS Sustain. Resour. Manag. 1 (2024) 1326–1339, https://doi.org/10.1016/10.1021/acssusresmgt.4c00003.
[37] A. Mukhopadhyay, M. Alipanah, L.A. Diaz, H. Jin, C. Barboza, C. House, Y. Fujita, V.S. Thompson, D.W. Reed, Electrochemically assisted (bio)leaching of end-of-life lithium-ion batteries for critical metals recovery, ACS Sustain. Chem. Eng. 12 (2024) 14119–14127, https://doi.org/10.1016/10.1021/acssuschemeng.4c06090.
[38] M. Saldaña, M. Jeldres, F.M. Galleguillos Madrid, S. Gallegos, I. Salazar, P. Robles, N. Toro, Bioleaching modeling-a review, Materials 16 (2023) 3812, https://doi.org/10.1016/10.3390/ma16103812.
[39] J. Petersen, From understanding the rate limitations of bioleaching mechanisms to improved bioleach process design, Hydrometallurgy 221 (2023) 106148 https://doi.org/10.1016/10.1016/j.hydromet.2023.106148.
[40] A. Sieber, L.R. Jelic, K. Kremser, G.M. Guebitz, Spent brewer's yeast as a selective biosorbent for metal recovery from polymetallic waste streams, Front. Bioeng. Biotechnol. 12 (2024) 1345112, https://doi.org/10.1016/10.3389/fbioe.2024.1345112.
[41] Jane Ferreira, Daniel Bertuol, Recovery of Nickel and Cobalt from Spent NiMH Batteries by Electrowinning, Chemical Engineering & Technology, 2012.
[42] S. Spiess, J. Kucera, T. Vaculovic, L. Birklbauer, C. Habermaier, A.S. Conde, M. Mandl, M. Haberbauer, Zinc recovery from bioleachate using a microbial electrolysis cell and comparison with selective precipitation, Front. Microbiol. 14 (2023) 1238853, https://doi.org/10.1016/10.3389/fmicb.2023.1238853.
[43] A. Keller, M.W. Hlawitschka, H.-J. Bart, Application of saponified D2EHPA for the selective extraction of manganese from spend lithium-ion batteries, Chem. Eng. Process. - Process. Intensif. 171 (2022) 108552 https://doi.org/10.1016/10.1016/j.cep.2021.108552.
[44] E. Gerold, S. Luidold, H. Antrekowitsch, Selective precipitation of metal oxalates from lithium ion battery leach solutions, Metals 10 (2020) 1435, https://doi.org/10.1016/10.3390/met10111435.
[45] J. Pavlović, S. Stopić, B. Friedrich, Z. Kamberović, Selective removal of heavy metals from metal-bearing wastewater in a cascade line reactor, Environ. Sci. Pollut. Res. Int. 14 (2007) 518–522, https://doi.org/10.1016/10.1065/espr2006.09.345.
[46] L. Wiszniewski, I. Marschall, T. Hochsteiner, T. McFarlane Hoad, K. Doschek-Held, H. Raupenstrauch, Evaluating refractory material performance in pyrometallurgical recycling of lithium-ion batteries under a reducing atmosphere, Ceram. Int. (2024) https://doi.org/10.1016/10.1016/j.ceramint.2024.08.220.
[47] A. Schönberg, Mathematische Modellierung metallurgischer Prozesse: Induktive Erwärmung einer Graphitschüttung, 2014.
[48] H. Raupenstrauch, A. Schönberg, S. Windisch, C. Ponak, V. Mally, A. Holzer WO 2021/175703 A1, 2021.
[49] C. Ponak, Carbo-thermal reduction of basic oxygen furnace slags with simultaneous removal of phosphorus via the gas phase. Dissertation, Leoben, 2019.
[50] A. Holzer, J. Zimmermann, L. Wiszniewski, T. Necke, C. Gatschlhofer, W. Öfner, H. Raupenstrauch, A combined hydro-mechanical and pyrometallurgical recycling approach to recover valuable metals from lithium-ion batteries avoiding lithium slagging, Batteries 9 (2023) 15, https://doi.org/10.1016/10.3390/batteries9010015.
[51] S. Mei, Q. Wang, M. Hao, J. Xu, H. Yin, H. Xiao, C. Feng, L. Jiang, X. Wang, F. Liu, X. Xu, Z. Wang, Theoretical analysis of induction heating in high-temperature epitaxial growth system, AIP Advances 8, 085114. https://doi.org/10.1016/10.1063/1.5030949.
[52] M. Rapf, H. Raupenstrauch, RecoPhos and other thermo-chemical processes for the recovery of phosphorus from sewage sludge, Proceeding to Depotech Conference, Leoben, Austria, 2012.
[53] N. Al Azri, R. Patel, G. Ozbuyukkaya, C. Kowall, G. Cormack, N. Proust, R. Enick, G. Veser, Batch-to-Continuous transition in the specialty chemicals Industry: Impact of operational differences on the production of dispersants, Chem. Eng. J. 445 (2022) 136775 https://doi.org/10.1016/10.1016/j.cej.2022.136775.
[54] W. Yin, K. Chen, Effect of the particle size and microstructure characteristics of the sample from HPGR on column bioleaching of agglomerated copper ore, Hydrometallurgy 200 (2021) 105563 https://doi.org/10.1016/10.1016/j.hydromet.2021.105563.
[55] L. Lalropuia, J. Kucera, W.Y. Rassy, E. Pakostova, D. Schild, M. Mandl, K. Kremser, G.M. Guebitz, Metal recovery from spent lithium-ion batteries via two-step bioleaching using adapted chemolithotrophs from an acidic mine pit lake, Front. Microbiol. 15 (2024) 1347072, https://doi.org/10.1016/10.3389/fmicb.2024.1347072.
[56] I. Ňancucheo, O.F. Rowe, S. Hedrich, D.B. Johnson, Solid and liquid media for isolating and cultivating acidophilic and acid-tolerant sulfate-reducing bacteria, FEMS Microbiol. Lett. 363 (2016) https://doi.org/10.1016/10.1093/femsle/fnw083.
[57] L. Wiszniewski, C. Gatschlhofer, A. Krammer, T. Hochsteiner, A. Holzer, H. Raupenstrauch, Influences of Pre-treatment Steps and Contaminants in a Pyrometallurgical Recycling Process for NCA (LiNi0.8Co0.15Al0.05O2) Lithium-Ion Battery Material, Livingstone, Sambia, 2023.
[58] L. Wiszniewski, Z. Raonic, B. Nuraeni, I. Marschall, B. Satritama, A. Rhamdhani, S. Riesel, Investigation of thermokinetics in carbo- and aluminothermic reduction of synthesized lithium iron phosphate black mass, 2024.
[59] M.E. Schlesinger, The thermodynamic properties of phosphorus and solid binary phosphides, Chem. Rev. 102 (2002) 4267–4301, https://doi.org/10.1016/10.1021/cr000039m.
[60] S. Lee, M. Song, S. Kim, V. Mathew, B. Sambandam, J.-Y. Hwang, J. Kim, High lithium storage properties in a manganese sulfide anode via an intercalation-cum-conversion reaction, J. Mater. Chem. A 8 (2020) 17537–17549, https://doi.org/10.1016/10.1039/D0TA05758D.
[61] M. Song, J.-Y. Hwang, J. Kim, Mns@N/S-C anode electrode with high lithium storage property by simple polyol refluxing method, Meet. Abstr. MA 2022 (01) (2022) 523, https://doi.org/10.1016/10.1149/MA2022-014523mtgabs.
[62] S. Feng, B. Chen, H. Chen, J. Yang, L. Ma, Y. Zhang, H. Li, S. Zeng, L. Xu, Facile coupling MnS nanoparticles with nitrogen, sulfur-doped carbon microsheet with improved Li-storage performance, Ionics 29 (2023) 2637–2646, https://doi.org/10.1016/10.1007/s11581-023-05059-y.
[63] W. Li, S. Lee, A. Manthiram, High-Nickel NMA: a cobalt-free alternative to NMC and NCA cathodes for lithium-ion batteries, Adv. Mater. 32 (2020) e2002718 https://doi.org/10.1016/10.1002/adma.202002718.
[64] F. MATSUNO, S. NISHIKIDA, H. IKESAKI, Mechanical properties of manganese sulphides in the temperature range between room temperature and 1000.DEG.C, ISIJ Int 25 (1985) 989–998, https://doi.org/10.1016/10.2355/isijinternational1966.25.989.
[65] Y. You, J. Kim, C. Kwakernaak, J.C. Brouwer, R. Westerwaal, W.G. Sloof, Surface oxidation and wettability of Fe–Mn and Fe–Mn–Si-alloyed steel after annealing, Met. Mater. Trans. A 54 (2023) 97–105, https://doi.org/10.1016/10.1007/s11661-022-06847-3.
[66] V.A. Lashgari, G. Zimbitas, C. Kwakernaak, W.G. Sloof, Kinetics of internal oxidation of Mn-Steel Alloys, Oxid. Met 82 (2014) 249–269, https://doi.org/10.1016/10.1007/s11085-014-9490-7.
[67] X. Zhang, C. Da Corrêa Silva, C. Liu, M. Prabhakar, M. Rohwerder, Selective oxidation of ternary Fe-Mn-Si alloys during annealing process, Corros. Sci. 174 (2020) 108859 https://doi.org/10.1016/10.1016/j.corsci.2020.108859.
[68] J. Wang, M. Xia, J. Wu, C. Ge, Ladle nozzle clogging in vacuum induction melting gas atomization: influence of the melt viscosity, Met. Mater. Trans. B 53 (2022) 2386–2397, https://doi.org/10.1016/10.1007/s11663-022-02537-y.
[69] A. Weicht, L. Achelis, M. Peters, V. Uhlenwinkel, U. Fritsching, Influence of Heated Gas on Atomization of Highly Viscous Melts, in:
[70] B. Xin, Di Zhang, X. Zhang, Y. Xia, F. Wu, S. Chen, L. Li, Bioleaching mechanism of Co and Li from spent lithium-ion battery by the mixed culture of acidophilic sulfur-oxidizing and iron-oxidizing bacteria, Bioresour. Technol. 100 (2009) 6163–6169, https://doi.org/10.1016/10.1016/j.biortech.2009.06.086.
[71] S. Yun, H. Jung, H.J. Lee, Y. Yang, J.S. Lee, M. Hur, B. Lee, J. Ahn, G. Hwang, Bioleaching of valuable metals from three cathode active materials comprising

lithium nickel cobalt manganese (NCM) oxide using indigenous microorganisms, J. Ind. Eng. Chem. 135 (2024) 552–560, https://doi.org/10.1016/10.1016/j.jiec.2024.01.067.
[72] S. Zhu, W. He, G. Li, X. Zhou, X. Zhang, J. Huang, Recovery of Co and Li from spent lithium-ion batteries by combination method of acid leaching and chemical precipitation, Trans. Nonferrous Met. Soc. China 22 (2012) 2274–2281, https://doi.org/10.1016/10.1016/S1003-6326(11)61460-X.
[73] T. Naseri, N. Bahaloo-Horeh, S.M. Mousavi, Bacterial leaching as a green approach for typical metals recovery from end-of-life coin cells batteries, J. Clean. Prod. 220 (2019) 483–492, https://doi.org/10.1016/10.1016/j.jclepro.2019.02.177.
[74] Z. Niu, Y. Zou, B. Xin, S. Chen, C. Liu, Y. Li, Process controls for improving bioleaching performance of both Li and Co from spent lithium ion batteries at high pulp density and its thermodynamics and kinetics exploration, Chemosphere 109 (2014) 92–98, https://doi.org/10.1016/10.1016/j.chemosphere.2014.02.059.
[75] Z. Liu, X. Liao, Y. Zhang, S. Li, M. Ye, Q. Gan, X. Fang, Z. Mo, Y. Huang, Z. Liang, W. Dai, S. Sun, A highly efficient process to enhance the bioleaching of spent lithium-ion batteries by bifunctional pyrite combined with elemental sulfur, J. Environ. Manag. 351 (2024) 119954 https://doi.org/10.1016/10.1016/j.jenvman.2023.119954.
[76] Q. Jing, J. Zhang, Y. Liu, C. Yang, B. Ma, Y. Chen, C. Wang, E-pH diagrams for the Li-Fe-P-H 2 O System from 298 to 473 K: thermodynamic analysis and application to the wet chemical processes of the LiFePO 4 cathode material, J. Phys. Chem. C. 123 (2019) 14207–14215, https://doi.org/10.1016/10.1021/acs.jpcc.9b02074.
[77] M. Arshadi, S.M. Mousavi, Simultaneous recovery of Ni and Cu from computer-printed circuit boards using bioleaching: statistical evaluation and optimization, Bioresour. Technol. 174 (2014) 233–242, https://doi.org/10.1016/10.1016/j.biortech.2014.09.140.
[78] M. GAN, M. LI, J. ZENG, X. LIU, J. ZHU, Y. HU, G. QIU, Acidithiobacillus ferrooxidans enhanced heavy metals immobilization efficiency in acidic aqueous system through bio-mediated coprecipitation, Trans. Nonferrous Met. Soc. China 27 (2017) 1156–1164, https://doi.org/10.1016/S1003-6326(17)60135-3.
[79] J. Sun, W. Zhou, L. Zhang, H. Cheng, Y. Wang, R. Tang, H. Zhou, Bioleaching of copper-containing electroplating sludge, J. Environ. Manag. 285 (2021) 112133 https://doi.org/10.1016/10.1016/j.jenvman.2021.112133.
[80] N.J. Boxall, K.Y. Cheng, W. Bruckard, A.H. Kaksonen, Application of indirect non-contact bioleaching for extracting metals from waste lithium-ion batteries, J. Hazard. Mater. 360 (2018) 504–511, https://doi.org/10.1016/10.1016/j.jhazmat.2018.08.024.
[81] T. Naseri, S.M. Mousavi, Improvement of Li and Mn bioleaching from spent lithium-ion batteries, using step-wise addition of biogenic sulfuric acid by Acidithiobacillus thiooxidans, Heliyon 10 (2024) e37447 https://doi.org/10.1016/10.1016/j.heliyon.2024.e37447.
[82] P.A. Olubambi, J.H. Potgieter, S. Ndlovu, J.O. Borode, Electrochemical studies on interplay of mineralogical variation and particle size on bioleaching low grade complex sulphide ores, Trans. Nonferrous Met. Soc. China 19 (2009) 1312–1325, https://doi.org/10.1016/10.1016/S1003-6326(08)60443-4.
[83] Y. Ma, M. Svärd, X. Xiao, J.M. Gardner, R.T. Olsson, K. Forsberg, Precipitation and crystallization used in the production of metal salts for Li-Ion battery materials: a review, Metals 10 (2020) 1609, https://doi.org/10.1016/10.3390/met10121609.
[84] J. Neumann, S. Nowak, M. Petranikova, M. Meeus, J.D. Gamarra, R. Younesi, M. Winter, Recycling of lithium-ion batteries current state of the art, circular economy, and next generation recycling, Adv. Energy Mater. (Internet) 12 (2022) 1–26.
[85] Z. Han, J. Li, W. Guan, Z. Cao, Q. Li, M. Wang, S. Wu, G. Zhang, Complete recovery of valuable metals from chlorinated titanium-white waste acids: Focus on solvent extraction for recovery and preparation of battery-grade manganese sulfate (MnSO4·H2O) from lab to pilot scale, Chem. Eng. J. 491 (2024) 151766 https://doi.org/10.1016/10.1016/j.cej.2024.151766.
[86] S.H. Joo, J. Kang, K. Woong, S.M. Shin, Production of chemical manganese dioxide from lithium ion battery ternary cathodic material by selective oxidative precipitation of manganese, Mater. Trans. 54 (2013) 844–849, https://doi.org/10.1016/10.2320/matertrans.M2012379.
[87] T. Tawonezvi, D. Zide, M. Nomnqa, M. Madondo, L. Petrik, B.J. Bladergroen, Recovery of NixMnyCoz(OH)2 and Li2CO3 from spent Li-ionB cathode leachates using non-Na precipitant-based chemical precipitation for sustainable recycling, Chem. Eng. J. Adv. 17 (2024) 100582 https://doi.org/10.1016/10.1016/j.ceja.2023.100582.
[88] H. Rostami, J. Valio, P. Tynjälä, U. Lassi, P. Suominen, Life cycle of LiFePO4 batteries: production, recycling, and market trends, ChemPhysChem 25 (2024) e202400459 https://doi.org/10.1016/10.1002/cphc.202400459.
[89] European Parliament, REGULATION (EU) 2023/1542 OF the European parliament and of the council of 12 July 2023 concerning batteries and waste batteries, amending Directive 2008/98/EC and Regulation (EU) 2019/1020 and repealing Directive 2006/66/EC, 2023.
[90] European Parliament, Proposal for a Regulation of the European parliament and of the council establishing a framework for ensuring a secure and sustainable supply of critical raw materials and amending Regulations (EU) 168/2013, (EU) 2018/858, 2018/1724 and (EU) 2019/1020, 2023.
[91] Y. Feng, Y. Xie, L. Yang, G. Yang, F. Han, K. Chen, P. Shao, G. He, X. Luo, Precise recovery of highly-purified iron phosphate from complex lithium extraction slag leach solution: theory guiding experiment, Sep. Purif. Technol. 347 (2024) 127605 https://doi.org/10.1016/10.1016/j.seppur.2024.127605.